AIP Advances

# Fourier–physical space coherent structure in flame–vortex interactions relevant to flame–turbulence interactions using a new signal periodization procedure

Cite as: AIP Advances **11**, 045006 (2021); https://doi.org/10.1063/5.0050280
Submitted: 11 March 2021 • Accepted: 16 March 2021 • Published Online: 02 April 2021

Paulo L. K. Paes, James G. Brasseur, Yuan Xuan, et al.

View Online Export Citation CrossMark

ARTICLES YOU MAY BE INTERESTED IN

Nanopatterned metallic transparent electrodes for the near-infrared spectrum
AIP Advances **11**, 045005 (2021); https://doi.org/10.1063/5.0044447

Magneto-hydrodynamics (MHD) flow analysis with mixed convection moves through a stretching surface
AIP Advances **11**, 045001 (2021); https://doi.org/10.1063/5.0047213

Numerical study of a Whitham equation exhibiting both breaking waves and continuous solutions
AIP Advances **11**, 045002 (2021); https://doi.org/10.1063/5.0047582

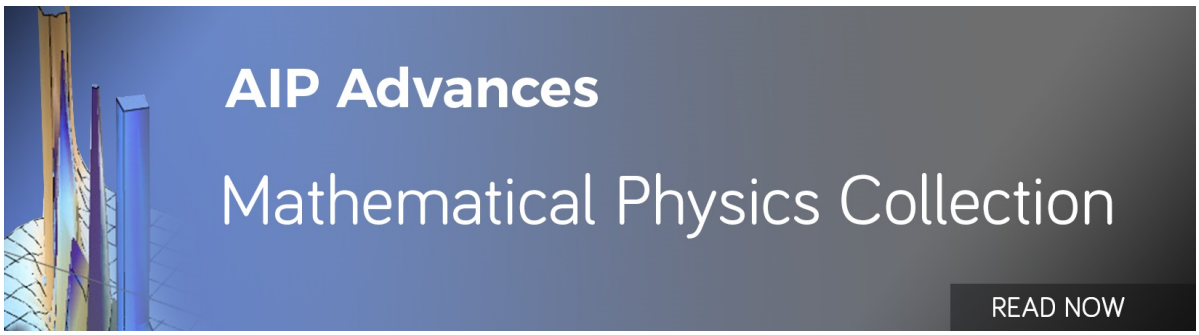


AIP Publishing



© 2021 Author(s).

# Fourier–physical space coherent structure in flame–vortex interactions relevant to flame–turbulence interactions using a new signal periodization procedure

Cite as: AIP Advances 11, 045006 (2021); doi: 10.1063/5.0050280
Submitted: 11 March 2021 • Accepted: 16 March 2021 •
Published Online: 2 April 2021

View Online Export Citation CrossMark

Paulo L. K. Paes,[1] James G. Brasseur,[1,2,a)] Yuan Xuan,[1] and Yash G. Shah[1]

## AFFILIATIONS

[1] Department of Mechanical Engineering, The Pennsylvania State University, University Park, Pennsylvania 16802, USA
[2] Smead Department of Aerospace Engineering Sciences, University of Colorado, Boulder, Colorado 80309, USA

[a)] **Author to whom correspondence should be addressed:** brasseur@colorado.edu

## ABSTRACT

The aim of the current study is to characterize key multidimensional relationships between coherent structures in physical vs Fourier/scale space representations of flame–turbulence interactions, as a basis for future analysis of the nonlinear couplings between key resolved scale (RS) and subfilter scale (SFS) motions in large-eddy simulation (LES) of premixed turbulent combustion. However, applying the bounded Fourier transform (FTF) in the nonperiodic flame-normal direction requires the removal of nonphysical Fourier content from the boundary discontinuities. To this end, we have developed a broadly applicable "discontinuity pollution removal" procedure for application to the FTF of multidimensional signals with a single nonperiodic direction. The procedure balances periodization of the signal near the boundaries with minimization of signal modification away from the boundaries. We applied the procedure in a physical–Fourier space analysis of the interactions between a flame and single-scale eddies modeled as the impact of a train of two-dimensional (2D) vortices on an initially planar premixed flame. We find that a specific spectrally broad localized coherent structure in Fourier space connects RS to SFS fluctuations in thermal energy and species concentration that, in physical space, are localized to the corrugations in the flame front in response to eddy–flame interactions. Within the RS fluctuations of energy and species concentration, the flame corrugation structure in physical space is found to be localized to sub-volumes within the RS region of 2D Fourier space. This new understanding of physical–Fourier space relationships categorizes classes of RS–SFS interactions relevant to SFS modeling in LES of premixed turbulent combustion.

*© 2021 Author(s). All article content, except where otherwise noted, is licensed under a Creative Commons Attribution (CC BY) license (http://creativecommons.org/licenses/by/4.0/).* https://doi.org/10.1063/5.0050280

## I. INTRODUCTION AND AIMS

The large-eddy simulation (LES) framework centers on decomposition in scale; LES modeling centers on the interactions between larger "resolved scale" (RS) and smaller "subfilter scale" (SFS) fluctuations in all dependent variables. When applied to premixed turbulent combustion, the reality of (practical) LES is that there necessarily exists key SFS chemical kinetics and thermo-mechanical dynamics that impact RS evolution but cannot be supported by the grid. Thus, unlike LES of incompressible turbulence, where only momentum dynamics are involved, LES modeling of strongly density-varying turbulent flows in the presence of chemical reaction and heat release must characterize key impacts of SFS fluctuations on the evolution of RS momentum, thermal energy, and concentrations of many chemically reacting species. In particular, SFS modeling is required for advective and chemical nonlinearities that couple the unresolvable evolutions of SFS variables with the evolution of RS variables supported by the effective grid. ("Effective" implies the existence of additional coarsening of the geometric grid from implicit filtering due to the dissipative content in the SFS models and numerical algorithm.) The central aim of our current research program is to ascertain the relationships between the coherent structure

in physical space and the coherent structure in Fourier space with data from reduced physics simulations that are designed to incorporate key dynamics from flame–turbulence interactions, ubiquitous in premixed turbulent combustion. As discussed in more detail in Sec. III A, this knowledge will be later used in analyses of key nonlinear RS–SFS couplings central to the evolution of coherent features of RS momentum, energy, and species concentration.

Our analysis centers on scale-based decomposition of the key dynamic variables. Decompositions such as proper orthogonal decomposition (POD)[1,2] and dynamic mode decomposition (DMD)[3] are therefore not useful for our needs. We choose the multidimensional Fourier decomposition for two primary reasons. First, the Fourier transform (FTF) is useful to decompose multidimensional multiscale analytic functions into a scale-based series of complex exponentials that are mathematically convenient for scale-based analysis in elemental form. The wavelet transform, for example, is a filtered version of the Fourier decomposition with Fourier modes grouped according to the choice of wavelet filter.[4] In multidimensional Fourier space, a Fourier mode is a complex harmonic function that is quantified with precisely defined scale (wavelength), direction (wavevector), amplitude, and phase (Fourier coefficient). Fourier decomposition of a continuous multiscale signal is "elemental" in the sense that whereas a single Fourier mode does not represent a physical space structure, collections of phase-correlated Fourier modes within localized volumes in Fourier space characterize a scale-based coherent structure in physical space, for example, through wavelet decomposition.[4–6] Each Fourier mode in the collection provides an elemental contribution to scale, strength, direction, and structure, with coherence determined by the phase relationships among the collection of Fourier modes.[4]

Multiscale nonlinear dynamical systems such as turbulence generally describe characteristic "scales of motion" statistically.[7] Local space–time analysis is required to relate spatial scales to coherent structural elements, such as vortex tubes and sheets, and local concentrations of turbulent kinetic energy, strain-rate, and vorticity.[8] However, once the local relationships of the scale-based turbulence structure between Fourier and physical space are understood, Fourier-based scale decomposition becomes a valuable tool to analyze the scale-based coherent structure and nonlinear interscale interactions in scale space in relationship to nonlinear interactions between scale-dependent coherent structures in physical space.[9]

Future publications will apply knowledge from the current kinematic study to analyze key dynamical nonlinearities in the equations of motion.[10] This direction for analysis creates the second, more important, reason for our application of Fourier scale decomposition: representation of a nonlinearity underlying interscale dynamics at its most elemental level. The FTF of the advective nonlinearities in the governing equations for momentum, energy, and species concentration in turbulent combustion, for example, appears as linear sums of elemental nonlinear "triadic" interactions among three Fourier modes with wave-vectors that form a closed triangle in multidimensional Fourier space.[9,11,12] In related studies,[10,13,14] we make use of this Fourier-spectral property to analyze the nonlinear interactions among scales of motion within turbulent-reacting flows in context with LES, where the turbulence structure is separated into RS and SFS spectral content. In the current study, we focus on the kinematic Fourier–physical space relationships that underlie the RS and SFS structure in flame–turbulence interactions.

Alternative approaches to scale-based decomposition apply basis functions that are mathematically more complex than the elemental Fourier basis. Examples include wavelet[15,16] and empirical mode[17] decomposition. The mathematical complexity of these basis functions, however, produces complicated representations of nonlinear terms in the transformed equations that greatly increase analytical complexity and reduce generality. The mathematical representation of nonlinear interactions among wavelet modes, for example, is a great deal more complex than the representations of elemental interactions among individual Fourier modes.[18,19] However, the wavelet transform of nonlinearities can be equivalently represented in Fourier space as sums of elemental nonlinear terms among filtered groupings of Fourier modes in localized volumes within multidimensional Fourier space. In that way, one can quantify the dynamical couplings between regions kinematically associated with different coherent features of the dynamical system. This is the approach we take here.

However, to develop this analysis, one must recognize and eliminate spurious spectral content that is introduced when the FTF is applied to a signal that is nonperiodic over a bounded domain. This is because the FTF of a bounded nonperiodic continuous analytic signal produces periodic extensions of the signal in physical space with discontinuities at the boundaries. As a global basis, the corresponding Fourier coefficients include contributions from these boundary discontinuities. In practice, signals from experimental measurements and numerical simulations are generally nonperiodic in at least one coordinate direction. Numerical simulations of flame–turbulence interactions in premixed turbulence combustion, for example, typically apply periodic boundary conditions in directions transverse to the mean flow, representing turbulence as statistically homogeneous in those directions; boundary discontinuities, therefore, do not exist in those directions. In contrast, in the flame-normal direction, the turbulence is statistically inhomogeneous and nonperiodic inflow/outflow boundary conditions are typically applied, creating boundary discontinuities in the periodically extended signal. However, computational and experimental signals are discretized, requiring the application of the discrete Fourier transform (DFT). The boundary "discontinuity" then becomes a large gradient with magnitude given by the jump in the signal between the inflow and outflow boundaries divided by the discretization scale. We shall continue to use the term "boundary discontinuity" to refer to the boundary gradients in discretized signals that characterize mathematical discontinuities in the corresponding continuous signal.

Nonperiodicity introduces an undesirable artifact in the Fourier transform that complicates scale-based analysis: Each boundary discontinuity creates Fourier coefficients with power-law decay extending from the lowest to highest wavenumber in the direction of the discontinuity. Consequently, when the highest physical gradients are resolved by the grid, the power-law artifact from the boundary discontinuity dominates the energy content of the physical signal at high wavenumbers. In the image processing literature,[20] the FTF of two-dimensional (2D) signals creates two power-law signatures referred to as "cross structure." Several methods have been proposed to overcome or minimize the impacts of this unwanted spectral content (pollution) from boundary


© Author(s) 2021

discontinuities, which overlaps the signal of interest in Fourier space (see Sec. II A). These methods are typically described as "periodization" procedures.

Classical methods to periodize signals include the application of smooth physical space filters at the non-periodic boundaries[21] and the antisymmetric signal extension[22] of the signal. Foucaut *et al.*[23] developed a method to remove the boundary discontinuities of experimental Particle Image Velocimetry (PIV) data by removing a straight line connecting first and last sample points of the signal and imposing anti-symmetry around the last sample point. Bruno *et al.*[24] developed a "Fourier continuation" method to periodize a signal within the Fourier framework by creating Fourier series within domains larger than the domain of the signal. Moisan[25] proposed a signal decomposition into a periodic component that resembles the original signal and a smooth component that captures the boundary discontinuities with linear functions within the domain, a step related to Foucaut *et al.*[23] as well as to the approach presented in Sec. II.

Whereas the methods described above retain spectral accuracy while removing spurious scale content by fully periodizing the signal, they also introduce new nonphysical Fourier content that overlaps with that of the original signal, making these approaches unsuitable for our applications. In particular, smooth filters at the non-periodic boundaries introduce new spectral content associated with the widowing filter. As we shall show (Secs. II B and II C), while the approaches from the work of Foucaut *et al.*[23] and Moisan[25] fully periodize the signal, they also modify the signal within the domain of interest at levels that are unacceptable for our application. Furthermore, whereas the antisymmetric signal extension removes $C^0$ discontinuities at the boundaries, it also introduces $C^1$ boundary discontinuities and makes the Fourier coefficients real-valued, masking phase information contained in the Fourier coefficients of the original signal and creating overlaps that cannot be removed. The "Fourier continuation" method introduces nonphysical large-scale Fourier content associated with the extension of the signal beyond its original domain, which overlaps with scales of interest in the original signal.

To overcome inadequacies of existing periodization methods for our application, we have developed a "pollution removal" methodology that specifically treats the tradeoff between full periodization and alteration of the signal in regions of interest (in Sec. II, we present a semi-empirical approach that removes pollution from boundary discontinuities without creating additional spurious content that overlaps the signal in regions of interest in both Fourier and physical space. This is done through user-based empiricism introduced to balance between the need to modify the signal near the boundaries for periodization with the extent to which the signal is modified away from the boundaries. We extend our method to higher order discontinuities in Appendix A and to multidimensional signals in Appendix B.

The current study aims to identify key Fourier–physical space relationships between coherent features in canonical flame–turbulence interactions. As discussed in Sec. III A, after applying the discontinuity pollution approach described here, we analyze the relationships between coherent structures in physical vs Fourier space using a reduced physics simulation that is designed to characterize key dynamical interactions between a chemically reacting flame and trains of single-scale eddies represented as 2D vortices. The specific objectives of the current paper are (1) to identify the spurious Fourier content created from nonphysical boundary discontinuities when the FTF is taken of nonperiodic variables on a bounded domain and develop a procedure to systematically remove the spurious content (pollution) from the boundary discontinuities without significantly altering the signal away from the boundaries, (2) to develop a reduced physics simulation of the interaction between an initially unstretched flame and a train of vortices and apply the simulation to validate the discontinuity-pollution-removal method, and (3) to analyze the 2D flame–vortex interaction model concurrently in Fourier and physical space to characterize the kinematic relationships between the localized coherent structure in physical space and the localized coherent structure in Fourier space within the LES framework.

The paper is organized as follows: Sec. II presents the mathematical representation underlying the Fourier description of nonperiodic signals over finite domains and the proposed "discontinuity pollution removal" procedure for one-dimensional (1D) signals. The procedure is extended to multidimensional signals in Appendixes B and C validated using reduced-physics simulations of 2D flame–vortex–train interactions (referred to henceforth as flame–vortex interactions). In Sec. III A, we present the concepts underlying the applicability of the flame–vortex interaction model to flame–turbulence interactions before describing the reduced physics model in Sec. III B. This is followed in Sec. III C with an analysis of the coherent structure of flame–vortex interactions in physical space. The Fourier space counterpart of coherent structure analysis is presented in Sec. IV using systematic spectral filtering. The relative contributions of distinct physical–Fourier space coherent structures to the energy content of distinct signals in context with the LES framework are analyzed in Sec. IV D. The key findings are discussed in Sec. V.

## II. REMOVAL OF POLLUTION IN THE FOURIER TRANSFORM OF NONPERIODIC SIGNALS OVER FINITE DOMAINS

In this section, we make use of Fourier theory to provide a better understanding of issues and implications of Fourier decomposition of nonperiodic signals over a finite domain. This analysis provides the foundation for the proposed "discontinuity pollution removal" procedure.

### A. The issues with Fourier decomposition of nonperiodic signals

As discussed in Sec. I, because the Fourier basis is unbounded, the FTF of a continuous function on a bounded domain includes periodic extensions of the function to infinity in all coordinate directions. In directions where the signal is not periodic, therefore, the periodically extended signal includes discontinuities at the boundaries that are reflected in the complete set of discrete Fourier coefficients. When the discrete FTF is applied to discretized nonperiodic functions, the infinite derivatives at the boundary discontinuities are now large-but-finite derivatives that are determined by the extent of jump together with grid resolution at the boundaries. The discontinuities at the boundaries between the function and its periodic extension may appear at the function level ($C^0$) but also in higher order derivatives $f^{(m)}(x) = d^m f/dx^m$ with $m \geq 1$, where the superscript $^{(m)}$ indicates the derivative.


© Author(s) 2021

To illustrate, consider the 1D bounded function $f(x)$ shown in Fig. 1, constructed by combining a cosine function with characteristic length scale $\ell$ with a Gaussian function with length scale $\eta$. With this function, we create three 1D signals defined over finite domains $L_1 = 6\ell$, $L_2 = 4.998\ell$, and $L_3 = 5.598\ell$, which are indicated as $f_1$, $f_2$, and $f_3$, respectively. $\eta = L_1/36$ and $\xi = L_1/3$ for all three signals. Figures 1(a)–1(c) show periodic extensions of $f_1$, $f_2$, and $f_3$, where the solid black vertical lines indicate the periodically extended domain boundaries. By construction, the three signals have the same characteristic length scales but different finite domain sizes.

The three signals in Fig. 1 are designed to characterize three different levels of discontinuity: (a) is a periodic signal that is continuous in the function at all its derivatives at the boundaries, (b) is a nonperiodic signal with only a $C^0$ discontinuity at the boundaries, and (c) is a nonperiodic signal with $C^0$ and $C^1$ boundary discontinuities. The jumps in boundary values (discontinuities) in the periodic extension of nonperiodic signals $f_2$ and $f_3$ are indicated by the vertical dashed lines at the boundaries in Figs. 1(b) and 1(c), respectively. These represent the boundary discontinuities at the function level $C^0$. $f_3$ discontinuities have both $C^0$ and $C^1$ with jumps in boundary values of $f$ and its derivative $f^{(1)}(x) = df/dx$.

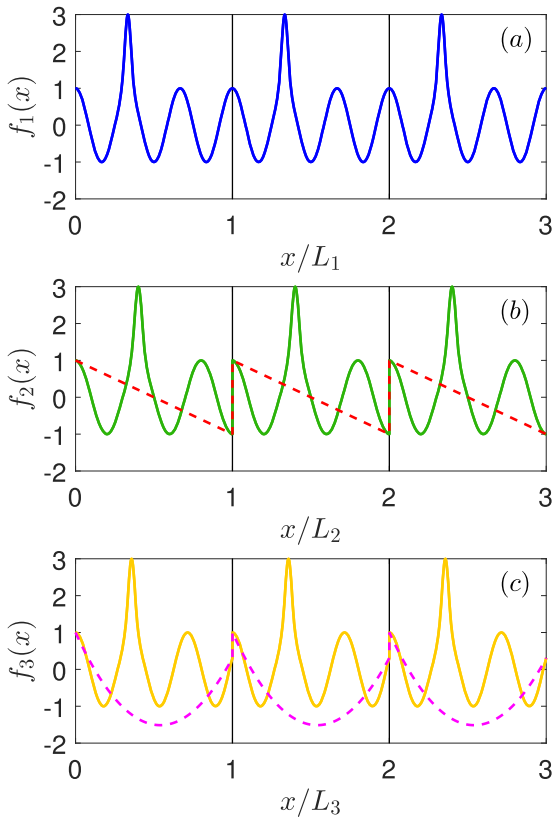


**FIG. 1.** Periodic extension of (a) $f_1$, (b) $f_2$, and (c) $f_3$, where $f(x) = \cos(\pi x/\ell) + 2e^{-((x-\xi)/\eta)^2}$, $L_1 = 6\ell$, $L_2 = 4.998\ell$, $L_3 = 5.598\ell$, $\eta = \ell/6 = L_1/36$, and $\xi = 2\ell = L_1/3$. The dashed red lines in (b) indicate the $C^0$ discontinuity function given by Eq. (3). The dashed magenta curve in (c) indicates the $C^0$ and $C^1$ boundary discontinuities derived in Appendix A.

The Fourier space spectrum of $f_1$, $f_2$, and $f_3$ in Figs. 1(a)–1(c) is shown in Fig. 2 where the wavenumber axis ($k_x$) is nondimensionalized with the cosine length scale $\ell$. The Fourier transform of the periodic signal (the blue curve in Fig. 2) has a spectral peak at $k_x\ell/\pi = 1$ and an exponential drop above the scale $\eta$ of the Gaussian function ($k_x\ell/\pi = \ell/\eta = 6$). In contrast, the Fourier content of signals $f_2$ and $f_3$ with nonperiodic boundary values (green and yellow curves in Fig. 2, respectively) has clear power-law decay of squared Fourier coefficients toward high wavenumbers with non-monotonic behavior surrounding a broad peak around $k_x\ell/\pi = 1$. We shall find that the difference between $\widehat{f_2}^2$ and $\widehat{f_3}^2$ at low wavenumbers ($k_x\ell/\pi \lesssim 4$) reflects the existence of the $C^1$ boundary discontinuity in $f_3$.

As shown in what follows, the boundary discontinuities presented in Figs. 1(b) and 1(c) have a broadband power-law Fourier energy content that overwhelms and pollutes the Fourier content of the original signal at scales of interest. In Fig. 2, for example, the power-law contribution from the $C^0$ boundary discontinuity in $f_2$ completely obscures the true signal $f_1$ at scales below the scale of the Gaussian function (i.e., $k_x\ell/\pi \gtrsim 6$) and pollutes the true signal at lower wavenumbers. Note that the discretization of the signal required to apply the FFT was chosen so that the cutoff in the power-law behavior at the discretization scale occurred at $k_x$ outside the range plotted in Fig. 2. Our aim is to remove the boundary-generated pollution shown in Fig. 2 without significantly interfering with the underlying signal of interest (blue curve) that we aim to recover in the pollution removal process.

To advance this aim, we quantify the Fourier coefficients of the boundary discontinuity from a nonperiodic signal. Consider an arbitrary smooth continuous 1D signal $f(x)$ over a finite domain $0 \le x \le L$ with boundary values $f(0)$ and $f(L)$. The periodic extension of $f(x)$ has a $C^0$ boundary discontinuity with boundary jump $\Delta f = f(L) - f(0)$. The bounded FTF of $f(x)$ is

$$\widehat{f}(k_x \neq 0) = \frac{1}{L}\int_0^L f(x)e^{-ik_x x}dx = -\frac{i}{k_x}\widehat{f'}(k_x) + \frac{i}{k_x}\frac{\Delta f}{L}, \qquad (1)$$

where $\widehat{f}(k_x)$ are the Fourier coefficients of $f(x)$ and $\widehat{f'}(k_x)$ are the Fourier coefficients of $f' = df/dx$, each a function of the infinite set of discrete wavenumbers, $k_x = k_n = 2\pi n/L, n = \pm 1, \ldots, \pm\infty$. $k_x = 0$ is

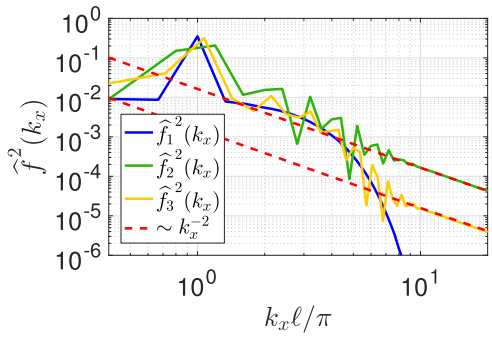


**FIG. 2.** Squared Fourier coefficients $\widehat{f_1}^2$ and $\widehat{f_2}^2$ over the wavenumber axis $k_x$ nondimensionalized by the scale $\ell$ of the cosine function (see Fig. 1). The dashed red line indicates the $C^0$ boundary discontinuity given by Eq. (2).


© Author(s) 2021

the average of $f(x)$ over the finite domain. The RHS of Eq. (1) was obtained using integration by parts and $e^{-ik_xL} = e^{-i2\pi n} = 1$.

The second term on the RHS of Eq. (1) isolates the Fourier content associated with the $C^0$ discontinuity in the periodic extension of $f(x)$. For periodic signals ($\Delta f = 0$), the second term does not contribute to the derivative of $f(x)$. For nonperiodic signals, the magnitude of this term follows a $k_x^{-1}$ power-law with amplitude proportional to $\Delta f$. Thus, the fundamental $C^0$ discontinuity function in Fourier space is described by

$$\widehat{d}(k_x) = \frac{i}{k_x}\frac{\Delta f}{L}, \quad for\ k_x \neq 0. \tag{2}$$

$\widehat{d}(0) = 0$ so that the discontinuity function does not contribute to the mean. The inverse FTF of $\widehat{d}(k_x)$ within the finite domain is

$$d(x) = \frac{\Delta f}{L}\left(x - \frac{L}{2}\right), \tag{3}$$

where $0 \le x \le L$. The physical space counterpart of Eq. (2) captures the fundamental $C^0$ discontinuity in $f(x)$ at the domain boundaries ($\Delta d = \Delta f$) with a linear sawtooth function extended periodically to infinity. The discontinuity function in physical and Fourier space is indicated by dashed red lines in Figs. 1(b) and 2 [with the mean included in $d(x)$ for better comparison with $f(x)$].

The linear sawtooth function in Eq. (3) captures only the $C^0$ boundary discontinuity in $f(x)$. In Appendix A, Eqs. (1)–(3) are generalized to $C^n$ discontinuities in the higher order derivatives $f^{(n)}(x) = d^n f/dx^n$ with $n = 0, 1, \ldots, N$. Like the discontinuity function for $f(x)$ given by Eq. (1), the discontinuity in the highest order derivative $f^{(N)}$ is represented in physical space by a linear discontinuity function $d_N^{(N)}(x)$ given by Eq. (A1). This function is sequentially integrated back to the 0th derivative level ($n = 0$) to produce an $N$th-order polynomial $d_N^{(0)}(x)$ that includes all discontinuities in $f^{(n)}(x)$ from the function level $n = 0$ up to the derivative level $n = N$. For example, a boundary discontinuity in $f^{(1)}(x) = df/dx$ is described by the linear discontinuity function $d_1^{(1)}(x)$ given by Eq. (A4) that when integrated to the function level produces the discontinuity function $d_1^{(0)}(x)$ given by Eq. (A6), the sum of parabolic plus linear functions.

In Fourier space, the sequential integration of $d_N^{(N)}(x)$ back to the $n = 0$ derivative level produces Fourier coefficients for $d_N^{(0)}(x)$ that follow a sum of power-laws $\sim k_x^{-(n+1)}$ with $n = 0, 1, \ldots, N$, given by Eq. (A12). The amplitude of each power-law is proportional to the magnitude of the boundary jump $\Delta f^{(n)} \equiv f^{(n)}(L) - f^{(n)}(0)$ at each derivative level, $n$. For example, the Fourier description of a function $f(x)$ with boundary discontinuities up to the first derivative level is given by [see Eq. (A12)]

$$\widehat{d_1^{(0)}}(k_x \neq 0) = \frac{\Delta f^{(0)}}{L}\left(\frac{i}{k_x}\right) + \frac{\Delta f^{(1)}}{L}\left(\frac{i}{k_x}\right)^2, \tag{4}$$

where $\Delta f^{(0)} = \Delta f$.

As an example, Fig. 3 shows the physical and Fourier space views of the $C^0$ and $C^1$ discontinuity functions of $f_3$ shown in Figs. 1(c) and 2. The boundary discontinuities are represented by mathematical expressions for $d_0^{(0)}(x)$ and $d_1^{(0)}(x)$ from boundary

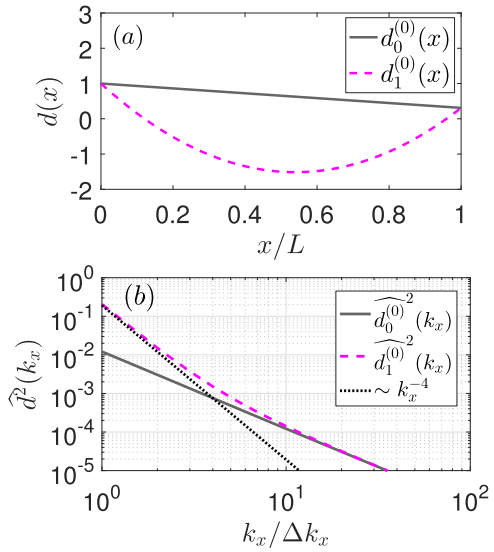


**FIG. 3.** (a) The physical space function and (b) the Fourier space spectral content of $d_0^{(0)}(x)$ and $d_1^{(0)}(x)$ derived in Appendix A to capture the $C^0$ and $C^0 + C^1$ boundary discontinuities for $f_3(x)$ shown in Fig. 1(c) having $\Delta f^{(0)} = -0.69$ and $\Delta f^{(1)} L_3 = 17.23$.

discontinuities in both the function $f(x)$ and its first derivative $f^{(1)}(x)$ (see Appendix A), that is, for both $C^0$ [Eqs. (2) and (3)] and $C^0 + C^1$ [Eqs. (4) and (A6)] boundary discontinuities in $f(x)$. In Fourier space [Fig. 3(b)], the squared Fourier coefficients of $d_1^{(0)}(x)$ follow a power-law $\sim k_x^{-2}$ in the high wavenumber limit and a different power-law $\sim k_x^{-4}$ in the low wavenumber limit, each associated with the Fourier representations of $C^0$ and $C^1$ discontinuity functions, respectively. In physical space [Fig. 3(a)], the parabolic function $d_1^{(0)}(x)$ captures the fundamental boundary discontinuities $C^0$ and $C^1$. Higher order boundary discontinuities do not exist since the function is smooth in derivatives above one. The linear function $d_0^{(0)}(x)$ captures only the fundamental boundary discontinuity $C^0$. The polynomials $d_N^{(0)}$ are constructed to capture the fundamental boundary discontinuity only up to $C^N$.

The fact that the higher order boundary discontinuities contain higher power-law exponents in $1/k_x$ will turn out to be important in the application of the discontinuity pollution removal procedure discussed in Secs. II B and II C, where the discontinuity removal function $d_N^{(0)}(x)$ will be used to remove pollution in Fourier space associated with the boundary discontinuities in the function. As shown in Fig. 3(b), for example, the variance of the discontinuity removal function for a function with discontinuity in the function and its first derivative is dominated by the $C^1$ discontinuity at wavenumbers below 4 and the $C^0$ discontinuity at high wavenumbers. We shall show that discontinuity removal should be limited to higher wavenumbers where the $d_0^{(0)}$ discontinuity dominates by orders of magnitude over higher-order singularities. Thus, in practice, the pollution removal procedure generally needs only be applied to the $C^0$ boundary discontinuity. This is the case in the current study.


© Author(s) 2021

### B. Pollution in the Fourier representation of a physical nonperiodic signal

In Fig. 4, we illustrate the spectral pollution with a physically relevant 1D signal obtained from a 2D simulation described in Sec. III B of the interaction between a laminar flame and a train of counter-rotating 2D vortices. Inflow/outflow boundary conditions are applied across a domain length of $16D$, where $D$ is the diameter of the individual vortices within the train. The blue curve in Fig. 4(a) is the streamwise momentum component along a pencil between the inflow and outflow boundaries. The flame, identified by the peak at $x/D = 4$, produces the largest physical gradient at the smallest physical scale, the flame scale, $\delta_f$. In Fig. 4(b), we plot, with the blue curve, the Fourier spectral content of the bounded 1D signal in Fig. 4(a) (blue curve).

As discussed above, Fig. 4 demonstrates that the bounded FTF of a continuous nonperiodic signal produces $C^0$ boundary discontinuities in physical space with the corresponding $k^{-2}$ broadband spectral energy content from the first wavenumber to $k_{max} \approx \pi/\Delta x$ [Eq. (2)]. The Direct Numerical Simulation (DNS) of turbulence requires that $\Delta x$ resolves well the smallest dynamically relevant viscous scale so that the physical signal has a viscous spectral roll-off that initiates at a scale an order of magnitude larger than the grid scale. As shown by the blue curve in Fig. 4(b), this roll-off is masked by the power-law content of the $C^0$ boundary discontinuity that overwhelms the frictional scale content at higher wavenumbers and that competes with physically relevant content at lower wavenumbers. The aim is to remove this pollution and uncover the small-scale content masked by the $C^0$ power-law at high wavenumbers.

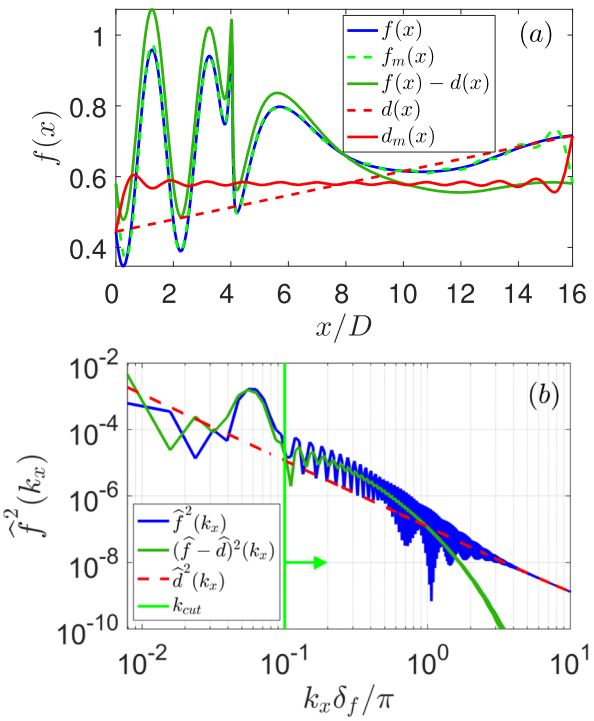


**FIG. 4.** (a) Physical and (b) Fourier space views of 1D signal extracted from 2D flame–vortex simulations described in IIIB. The blue curves show the original signal, the dashed red curves indicate the expressions that capture the fundamental $C^0$ boundary discontinuities [Eqs. (3) and (2)], and the dark green curves show the "periodized" signal after removing the later from the former. The mean $f(x)$ is added to $d(x)$ for better comparison. The dashed green curve in (a) indicates the post-processed signal discussed in Sec. II C using the filter cutoff wavenumber $k_{cut}$ indicated by a vertical green line in (b).

If one simply removed $\widehat{d}(k_x)$ given by Eq. (2) from the discrete FTF of the original nonperiodic signal $f(x)$, the inverse transform $\widehat{f}(k_x) - \widehat{d}(k_x)$ would produce a periodized form of the blue signal in Fig. 4 with the fundamental $C^0$ boundary discontinuity removed. This fully periodized signal is shown in physical space by the solid green curve in Fig. 4(a) and the original blue curve with the sawtooth function in Fig. 4(a) subtracted (after shifting to zero mean). Because the sawtooth function includes the $C^0$ boundary discontinuity, the full removal of pollution from the boundary discontinuity is equivalent to full periodization, as noted in Refs. 23 and 25.

The squared Fourier coefficients of the periodized signal are shown in Fig. 4(b) with the solid green curve. Note that the curve has an exponential drop off beginning near the wavenumber corresponding to the flame length scale, indicating that the pollution at high wavenumbers corresponding to the discontinuity has been removed. This is particularly obvious at wavenumbers $k_x\delta_f/\pi \gtrsim 1$, where the $k^{-2}$ reduction in $\widehat{f}^2(k_x)$ dominates and fully masks the true signal. At wavenumbers below $k_x\delta_f/\pi \approx 1$, the Fourier coefficients associated with the signal dominate the coefficients associated with the discontinuity so that the signal is modified relatively little there. However, at wavenumbers $k_x\delta_f/\pi \lesssim 0.05$, the lowest four wavenumbers, the Fourier coefficients within the power-law drop contain variance that overlaps with the true signal. This modification at the lowest few wavenumbers results from subtracting the "ramp" part of the sawtooth function, the largest scale feature of the inverse transform of the discontinuity term $\widehat{d}(k_x)$ in Eq. (2). This content interferes with the true signal and modifies the overall shape of the function, as shown by comparing the blue and dark green curves in Fig. 4(a).

We find that in order to remove the $C^0$ boundary discontinuity from the signal $f(x)$ using the same $C^0$ discontinuity embedded in the sawtooth function $d(x)$, it was necessary to also change the signal globally over the domain. We further find from Fig. 4 that the extent of signal modification that is required to periodize the signal depends on the relative variance content of the signal vs sawtooth function at the lowest wavenumbers since the magnitude of the Fourier coefficients increases like $k_x^{-2}$. The lowest $k_x$ content that defines the overall shape of the largest-scale variations in the signal. In effect, by removing pollution at the highest wavenumbers that results from the $C^0$ boundary discontinuity from non-periodicity in $f(x)$, pollution is added at the lowest wavenumbers to account for the signal content in $d(x)$ between the boundaries at the very largest Fourier scales. In Sec. II C, we introduce a procedure for removing spurious signal content at the highest wavenumbers arising from the boundary discontinuity within $d(x)$ while minimizing modification of the signal of interest at the lowest wavenumbers. To do so, it requires a tradeoff that must be handled empirically.


© Author(s) 2021

### C. A proposed pollution removal procedure that balances periodicity with signal modification

Since the boundary discontinuity is associated with the highest wavenumbers, consider a high-pass-filtered version of the discontinuity function,

$$\widehat{d}_m(k_x;k_{cut}) = m(k_x;k_{cut})\widehat{d}(k_x), \tag{5}$$

where

$$m(k_x;k_{cut}) = \begin{cases} 1 & \text{if } |k_x| \geq k_{cut}, \\ 0 & \text{if } |k_x| < k_{cut}. \end{cases} \tag{6}$$

The inverse transform of $\widehat{d}_m(k_x)$, $d_m(x;k_{cut})$, is given in Fig. 5(a) for the three filter scales $k_{cut}$ shown in Fig. 5(b). The red dashed curve in Fig. 5(a) includes all Fourier coefficients ($k_{cut} = 0$). As $k_{cut}$ is systematically moved toward higher wavenumbers, $d_m(x;k_{cut})$ systematically localizes around the discontinuity at the domain boundaries the contribution from the center of the domain.

The concept is to modulate $f(x)$ by subtracting $d_m(x;k_{cut})$ rather than $d(x)$ to create the modulated function $f_m(x;k_{cut}) = f(x) - d_m(x;k_{cut})$. As just discussed, when $k_{cut} = 0$, all Fourier modes of $f(x)$ are modulated [$d_m(x;k_{cut}) = d(x)$], the boundary discontinuity is fully removed, and the signal is fully periodized; however, the modulated version $f(x) - d(x)$ has been modulated globally. In contrast, when $k_{cut} = k_{max}$, $f(x)$ is left unchanged [$d_m(x;k_{cut}) = 0$] and the signal remains fully nonperiodic. It is therefore not surprising to find that the jump in the modulated signal $f_m(x;k_{cut})$ depends on $k_{cut}$. This is shown in the inset of Fig. 5(a), where the degree of reduction in the boundary discontinuity $d_m(x;k_{cut})$ is shown to decrease with increasing $k_{cut}$. We note that the reduction is minimal when $k_{cut}\delta_f/\pi = 0.5$, just below the roll-off in the signal which, as shown in Fig. 4(b), occurs at $k_x\delta_f/\pi \approx 1$. We conclude that there is a tradeoff between the degree of reduction in the boundary discontinuity and periodization of the signal (pushing $k_{cut}$ to smaller values) and the minimization of signal modification away from the boundaries (pushing $k_{cut}$ to higher values).

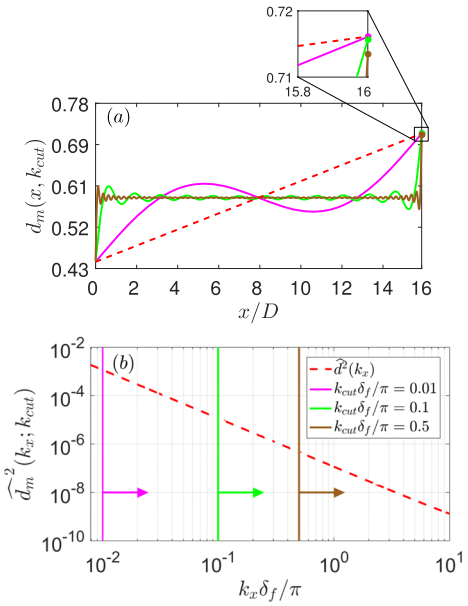


**FIG. 5.** (a) Physical and (b) Fourier space representation of modulated discontinuity $d_m(x;k_{cut})$ and $\widehat{d}_m(k_x;k_{cut})$, respectively, for three cutoff wavenumbers $k_{cut} > 0$ within the power-law spectrum of $\widehat{d}^2(k_x)$. The mean $f(x)$ is added to $d_m(x;k_{cut})$ for better comparison with Fig. 4. The inset of Fig. 5(a) shows boundary values for each $d_m(x;k_{cut})$.

In order to quantify the interplay between the degree of periodization vs the degree of modification of the original signal after removing $d_m(x;k_{cut})$ from $f(x)$, we define two parameters to quantify these two modulations. We then apply these two parameters within a "partial periodization" procedure that balances signal modulation with discontinuity removal. The first parameter is the ratio of content in the modulation function, $d_m(x;k_{cut})$, to the content in the original signal, $f(x)$, where "content" is defined with the $L^2$ norm,

$$\varepsilon(k_{cut}) = \frac{\|d_m(x;k_{cut})\|_V}{\|f(x)\|_V}. \tag{7}$$

The volume of interest, $V$, may be chosen as the entire domain or a subset of the domain, for example, to exclude boundary regions. $\varepsilon(k_{cut})$ quantifies the relative variance content removed from the original signal. In principle, the aim is to minimize this parameter. The second parameter quantifies the level of residual gradient at the boundary relative to the maximum physical gradient within the volume of interest,

$$\Delta_r(k_{cut}) = \frac{|\Delta f_m(k_{cut})|/\Delta x}{|max_x(\partial f(x)/\partial x)_V|}, \tag{8}$$

where

$$\Delta f_m(k_{cut}) = f_m(L,k_{cut}) - f_m(0,k_{cut}) = \Delta f - \Delta d_m(k_{cut}). \tag{9}$$

$\Delta f_m(k_{cut})$ is the residual boundary jump in the modified signal, and $\Delta f$ and $\Delta d_m(k_{cut})$ are the boundary jumps in the original signal and modified discontinuity function, respectively. Like $\varepsilon(k_{cut})$, the aim is to minimize $\Delta_r(k_{cut})$.

Consider Fig. 6, where the signal modification parameter $\varepsilon(k_{cut})$ and the residual jump parameter $\Delta_r(k_{cut})$ are plotted against nondimensional $k_{cut}$ for the physical signal shown in Fig. 4. The

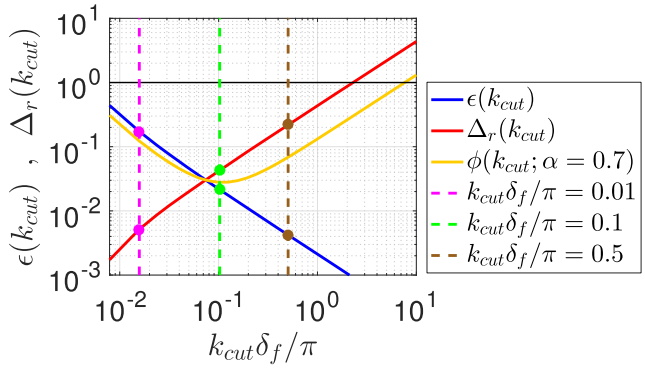


**FIG. 6.** Signal modification $\varepsilon(k_{cut})$ and residual discontinuity $\Delta_r(k_{cut})$ as a function of cutoff wavenumber $k_{cut}$ for the physical signal shown in Fig. 4.


© Author(s) 2021

dashed vertical lines indicate $k_{cut}$ associated with each $d_m(x;k_{cut})$ shown in Fig. 5, and the symbols indicate their respective $\varepsilon(k_{cut})$ and $\Delta_r(k_{cut})$ values. Both curves display approximate power-law dependencies that show the quantitative tradeoff between the minimization of the boundary discontinuity (smaller $k_{cut}$) and the minimization of signal modification (larger $k_{cut}$).

The fact that $\Delta_r(k_{cut})$, the red curve in Fig. 6, exceeds 1 at the highest values of $k_{cut}$ shows that the spurious gradient in $f(x)$ at the domain boundary exceeds the maximum physical gradient in $f(x)$ within the domain, reflecting major pollution in Fourier space at high wavenumbers, where in Fig. 4(b) the blue curve greatly exceeds the green curve. At these values of $k_{cut}$, the modified signal retains strong non-periodicity. In contrast, at the lowest value of $k_{cut}$ in Fig. 6, the red curve shows that the boundary discontinuity has been nearly entirely removed ($\Delta_r \approx 0.001$) and the modified signal is close to fully periodic; however, the blue curve shows major modifications to the original signal ($\varepsilon \approx 0.45$). However, at the crossover of the two curves, both the level of modification to the original function and the residual level of boundary discontinuity are reasonable, around 3%, suggesting that reasonable tradeoffs exist that can minimize both the pollution due to nonperiodicity and the degree of modification of the signal away from the boundaries, albeit with small residual levels of both remaining. This observation provides the basis for our proposed discontinuity pollution removal procedure.

The fundamental boundary discontinuity $\Delta f = f(L) - f(0)$ is represented in physical space by Eq. (3) and Fourier space by Eq. (2), a sawtooth function with zero mean and boundary discontinuities $\Delta d = d(L) - d(0)$ matching that of the function $f(x)$. The procedure to remove the discontinuity from the Fourier transform of $f(x)$ centers on the removal of Fourier content $\widehat{d}_m(k_x;k_{cut}) = m(k_x;k_{cut})\widehat{d}(k_x)$ from the original signal $\widehat{f}(k_x)$, where $m(k_x;k_{cut})$ is a high-pass filter over $k_x \geq k_{cut}$. Since the aim is to significantly modulate the signal only near the boundary discontinuity, $m(k_x;k_{cut})$ is designed to modify the signal over a to-be-determined range of high wavenumbers, which localizes to the boundary discontinuity to create $f_m(x;k_{cut}) \leftrightarrow \widehat{f}_m(k_x;k_{cut})) = \widehat{f}(k_x) - m(k_x;k_{cut})\widehat{d}(k_x)$.

The aim is to remove the spectral content associated with the boundary discontinuity without significant modification of the signal away from the boundaries. To identify an optimal filter cutoff wavenumber $k_{cut}^{opt}$ that provides the best tradeoff between the minimization of signal modification, $\varepsilon$, and minimization of the residual boundary discontinuity, $\Delta_r$, we define the following weighted variable:

$$\phi(k_{cut};\alpha) = \alpha\varepsilon(k_{cut}) + (1-\alpha)\Delta_r(k_{cut}), \tag{10}$$

where $0 < \alpha < 1$. $\alpha$ is a user-specific parameter that weights the relative contribution of $\varepsilon$ vs $\Delta_r$. The "optimal" filter cutoff wavenumber $k_{cut}^{opt}$ is defined as the minimum in $\phi(k_{cut};\alpha)$ as a function of $k_{cut}$ for specified fixed $\alpha$,

$$\phi(k_{cut}^{opt};\alpha) = min_{k_{cut}}[\phi(k_{cut};\alpha)]. \tag{11}$$

The choice of $\alpha$ depends on the characteristics of the original nonperiodic signal and the aims of the user. Large $\alpha$ favors the minimization of changes in the signal, while small $\alpha$ favors the minimization of the residual boundary discontinuity and the retained level of periodicity. Note that $\varepsilon$ and $\Delta_r$ [Eqs. (7) and (8)] involve integrals over a user-specified volume, $V$, allowing the user to decide the region of the signal where modulation should be minimized. In this section, we use the entire domain for $V$.

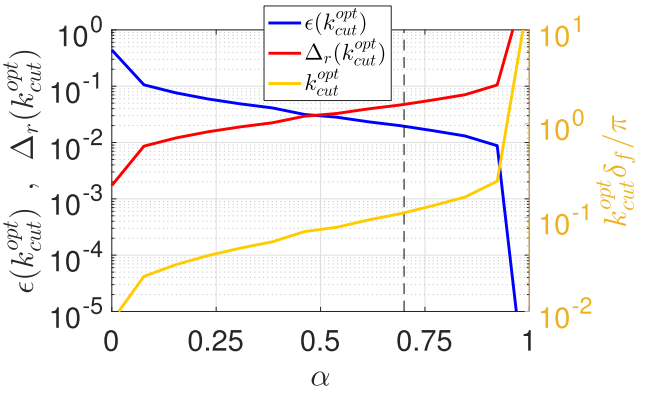


**FIG. 7.** $\varepsilon$ (magenta), $\Delta_r$ (blue), and $k_{cut}^{opt}$ (red) curves as a function of $\alpha$ for the 1D signal in Fig. 4 extracted from 2D flame–vortex interactions shown. The vertical dashed line is the value $\alpha = 0.7$ shown by the orange curve in Fig. 6.

To illustrate the tradeoffs in the selection of $\alpha$, Fig. 7 shows the dependence of $\varepsilon$, $\Delta_r$, and $k_{cut}^{opt}$ for different choices of $\alpha$ using the 1D signal in Fig. 4. Figure 4 shows that for each $\alpha$ there is a corresponding $k_{cut}^{opt}$ from the minimization of $\phi(k_{cut};\alpha)$, which is used to evaluate the tradeoffs between $\varepsilon$ and $\Delta_r$. For this signal if $\alpha$ were chosen as 0.7, for example (dashed line in Fig. 7), the signal modification would be limited to 2%, while the residual jump in the post-processed signal remains below 5%. The resulting weighted criterion curve $\phi(k_{cut};\alpha = 0.7)$ is shown in Fig. 6 by the orange curve, and the corresponding post-processed 1D signal using $k_{cut}^{opt}\delta_f/\pi = 0.1$ is indicated in Fig. 4(a) by the dashed green curve, $f_m(x)$.

In Appendix B, the discontinuity pollution removal procedure is extended to three-dimensional (3D) signals with one nonperiodic direction, and in Appendix C, a sensitivity analysis of $\alpha$ is performed to exemplify the identification of $\alpha$ in practical applications.

## III. COHERENT STRUCTURE IN FLAME–VORTEX INTERACTIONS AS A REDUCED PHYSICS MODEL OF FLAME–TURBULENCE INTERACTION

### A. Underlying concepts

Having developed a viable discontinuity pollution removal method, we are in a position to study scale-dependent coherent structure simultaneously in physical space and Fourier scale space. A central aim of the current study is to determine the relationships among key coherent elements in momentum, thermal energy, and species concentration from turbulence–flame interactions in terms of the characteristic scales of the coherent elements and their spatial inter-relationships concurrently in physical space and Fourier space. As discussed in Sec. I, we apply the Fourier spectral decomposition in part because the harmonic basis is explicitly scale-based, but specifically because the Fourier transform produces the most elemental description of the advective and chemical nonlinearities in the equations of motion as linear sums of nonlinear terms, each of which represents an elemental interaction among a few


© Author(s) 2021

Fourier modes. As will be described in future manuscripts,[10] these mathematically elegant elemental forms within the Fourier spectral description of nonlinear interscale interactions may be rearranged in order to down-select a small percentage of the most dominant nonlinear interscale couplings that contribute to the evolution of resolved scale momentum, thermal energy, and species concentration predicted in LES of flame–turbulence interactions. These are the dominant dynamical interactions that underlie the modeled terms in LES of premixed turbulent combustion. The current study of the relationship between coherent structure in physical and Fourier space provides the understanding of SFS vs RS coherent structure in relationship to the effective LES filter cutoff within the Fourier description of scale, as determined by effective grid. This understanding will inform future analyses and a new modeling strategy for the RS–SFS contributions to the nonlinear terms in LES of flame–turbulence interactions centered on the development physically meaningful mathematical forms for scale-dependent SFS variables.

However, the three-dimensional chaotic forcings of a thin flame by the full range of turbulence eddy scales create highly complex multiscale flame distortions in response to the wide ranges of eddy scales and strengths relative to the flame scale and flame strength local to a flame–eddy interaction. Spatial coherence resulting from these interactions is correspondingly highly complex with the coherent structure created over wide ranges of scale by the dynamics associated with the distorting flame. This complexity in multi-scale response makes it difficult to dissect the Fourier–physical space relationships created by groupings of eddies at similar scale and strength. To reduce the levels of complexity from the impacts of a full range of 3D turbulence eddying motions on flame dynamics, and to more clearly describe coherent structure physical–Fourier space relationships in context with flame topography, we have created a "reduced-physics" model that captures a key underlying element in turbulence–flame dynamics: the distortion of a flame in response to repetitive forcing by single-scale eddies of controlled scale and strength relative to a well-defined flame sheet. Specifically, we design controllable non-chaotic interactions between an initially unstretched planar flame sheet and topologically well-defined eddies modeled as trains of two-dimensional single-scale vortices with controlled scale and strength relative to that of the flame. We argue that this flame–vortex interaction model captures essential deformations of a flame sheet in response to single-scale eddy motion. The reduction in dimensional and physical complexity produces well-defined Fourier–physical space relationships in the coherent structure while retaining sufficient levels of complexity to apply the results extracts the key elements of turbulence–flame interactions that are local to flame–eddy interactions in premixed turbulent combustion.

With the reduced-physics flame–vortex interaction model, we are able to choose the relationships between the flame scale/strength and eddy scale/strength in relationship to the interactions between a subset of eddies within the full range of turbulence–flame interactions that are ubiquitous in premixed turbulent combustion. As discussed in Sec. III B, the current study focuses on eddies with a single length scale an order of magnitude larger than the characteristic flame scale. This ratio of vortex to flame scale is chosen because turbulence eddies of order the flame scale tend not to strongly impact flame distortion,[26] while the response to eddies larger in scale may be deduced from the current results. We argue that the current flame–eddy model characterizes local deformations of the flame sheet at the defined eddy scale with the degree of response determined by the strength of the defined single-scale eddies relative to the strength of the flame. In the complete series of studies underlying the current paper, relative eddy strengths are chosen to create "weak," "moderate," and "strong" response in flame deformation. In the current paper, we discuss in detail the "weak" response case, designed to create large repetitive distortions of the flame without pinching or the creation of pockets. The higher strength of the "moderate" case vortices was chosen to produce pinching (but no pockets), while the "strong" vortex case was designed to create repetitive pocket formation. Because the primary conclusions from this series of studies can be presented in context with "weak" case, we present detailed results for this case in the current paper. The "moderate" and "strong" cases are discussed in Sec. V in context with discussion of the application of the current analysis to 3D turbulence–flame interactions.

To apply the 2D Fourier description, the nonphysical spectral content from boundary discontinuities at boundaries is removed with the discontinuity pollution removal procedure described in Sec. II generalized to 3D signals (Appendixes B and C). With 2D spectral filtering, we identify the relationship between characteristic coherent features in physical and Fourier space associated with specific flame responses and we quantify the relative contributions of these features to the total variance content of key variables.

### B. Overview of numerical simulation

In turbulent premixed flames, stiff nonlinear chemical reactions involving many reacting scalars introduce broad ranges of length and time scales that overlap with the characteristic scales of turbulence motions, resulting in strong two-way couplings between turbulence and combustion.[27–29] These scales are typically organized in the form of key non-dimensional parameters within a parameter space that demarcates regimes of turbulent premixed combustion (Borghi,[27] Peters,[28] and Williams[29]).

The Karlovitz number is a key non-dimensional parameter that characterizes these regimes,

$$Ka \equiv \tau_F/\tau_\eta \sim \gamma(u_\eta/s_L)^2 \sim \gamma^{-1}\left(\delta_f/\eta\right)^2, \tag{12}$$

where $\tau_F = \delta_f/s_L$ is the characteristic flame time scale ($s_L$ and $\delta_f$ are the laminar flame speed and thickness, respectively), $\tau_\eta = \eta/u_\eta = \eta^2/\nu$ is the Kolmogorov time scale ($u_\eta$ and $\eta$ are the Kolmogorov velocity and length scales, respectively), and $\nu$ is the kinematic viscosity. In Eq. (12), $\gamma \equiv s_L\delta_f/\alpha \approx s_L\delta_f/\nu$, where $\alpha$ is the thermal diffusivity. $\alpha \approx \nu$ in air, even at high temperature and pressure. Assuming air, then, $\gamma \sim O(1)$ in the diffusion-dominated reaction zone. [In the inflow, where the temperature and kinematic viscosity are an order of magnitude lower, $\gamma \sim O(10)$ or higher.] $Ka \ll 1$ is traditionally described as the "flamelet" regime, while $1 \lesssim Ka \lesssim 10^2$ and $Ka \gtrsim 10^2$ are described as "thin," and "broken" or "distributed" reaction zone regimes, respectively.[27–29] Recent studies[26,30] suggest that the distributed combustion regime may be associated with higher $Ka \gtrsim O(10^4)$.


© Author(s) 2021

Some key fundamental dynamics of flame–turbulence interactions under distinct regimes may be conceptualized by reduced-physics systems that characterize local interactions between a premixed flame and single-scale turbulence eddies from within the inertial eddies within high Reynolds number turbulent reacting flow,[31] as illustrated experimentally in Filatyev *et al.*[32] Using this framework, we represent the interaction between a laminar flame and single-scale inertial eddies of length scale $r$ and velocity scale $u_r$ with a train of 2D vortices with vortex scale $l_v \sim r$ and velocity scale $u_v \sim u_r$. To estimate the Karlovitz number with vortex scales, we apply the classical Kolmogorov 1941 scaling ($\varepsilon \sim u_v^3/l_v$) to Eq. (12) to obtain

$$Ka \sim \left(l_v/\delta_f\right)^{-1}\left(u_v/S_L\right)\left(Re_v\right)^{1/2}, \tag{13}$$

where $Re_v = u_v l_v/\nu$ is the vortex Reynolds number in the unburnt mixture, and we model the vortices as characteristic inertial-range turbulence eddies.

In the numerical model, a vortex train was designed to characterize inertial-range eddies on the reactant side of high $Ka$ turbulent premixed flames in the thin reaction zone regime[30] with an integral scale Reynolds number of $\sim 10^4$ and an Karlovitz number of $\sim 1$, respectively. The vortex length scale was purposefully chosen to be an order of magnitude larger than the flame length scale ($l_v/\delta_f \approx 10$) to characterize the impacts of larger inertial range eddies and to better elucidate characteristics at disparate vortex and flame scales in Fourier space. The square of the vortex to flame velocity ratio, $(u_v/s_L)^2$, characterizes the ratio of vortex to flame strength. For the "weak" vortex case discussed in the current paper, $u_v/s_L \approx 0.5$.

As discussed in Sec. III A, whereas we discuss the key results in context with the weak case simulation, we also developed "moderate" and "strong" vortex simulations with $u_v/s_L \approx 2$ and 5, respectively. Whereas the weak case was designed to create strong repetitive distortions of the flame sheet, the moderate case was designed to create "pinching" distortions, while the strong case was designed to create repetitive pinching and pocket formation. Most of the new knowledge from these studies was obtained with the weak case. As will be discussed in Sec. V, the strong case adds insight relevant to the application of these analysis to turbulence–flame interactions.

Table I summarizes relevant simulation parameters with the vortices at the location of the flame front in a corresponding cold-flow simulation. $\delta_f$ is defined as the distance between the iso-levels of 5% and 85% of the progress variable $C = (T - T_u)/(T_b - T_u)$, where $T_u$ and $T_b$ are the temperatures in the unburnt and burnt mixtures, respectively. The thermochemical conditions in the unburnt mixture (subscript $u$) shown in Table I are selected according to those used in the experiments of moderate Ka turbulent premixed flames by Skiba *et al.*[30]

**TABLE I.** Important parameters for the flame–vortex interaction simulation.

| | | |
|---|---|---|
| Pressure | $p$ | 1 bar |
| Unburnt temperature | $T_u$ | 300 K |
| Unburnt equivalence ratio | $\phi_u$ | 1 |
| Laminar flame thickness | $\delta_f$ | 0.5 mm |
| Laminar flame burning speed | $S_L$ | 39 cm/s |
| Vortex diameter | $D$ | 7.9 mm |
| Vortex length scale | $l_v$ | 5 mm |
| Vortex velocity scale | $u_v$ | 19 cm/s |
| Length scale ratio | $l_v/\delta_f$ | 10 |
| Velocity scale ratio | $u_v/s_L$ | 0.5 |
| Vortex Reynolds number | $Re_v$ | 250 |
| Karlovitz number | $Ka$ | 2.5 |

The 2D numerical simulation was performed within the rectangular domain illustrated in Fig. 8, with domain lengths $L_y = 4D$ and $L_x = 16D$ in the cross-stream and streamwise directions, respectively, where $D$ is the vortex diameter. At the initiation of the simulation, a pre-computed planar $n$-heptane/air laminar premixed flame was placed four vortex diameters downstream of the inflow boundary. An inflow of unburnt $n$-heptane/air mixture is injected into the domain in the streamwise direction $x$, and the burnt products exit through the outflow plane. Periodic boundary conditions are applied in the cross-stream direction. An array of counter-rotating vortex pairs is continuously injected, with specified mean inflow velocity, in the inflow boundary using time-varying Dirichlet boundary conditions for the velocity components. The convective outflow[33] is enforced in the outflow boundary.

The array of vortices is kinematically constructed from a combination of two Fourier modes (and their complex conjugates) as shown in 2D Fourier space in Fig. 9(b). The vector Fourier coefficients, perpendicular to the two primary wavevectors shown in Fig. 9(b) to satisfy incompressibility, are aligned in opposite directions. This combination produces an spatial array of single-scale counter-rotating vortices with circulation in opposite directions and with zero average linear or swirl velocity, as described in the work of Brasseur and Wang.[5] Figure 9(a) shows a 2D isocontour of a normalized velocity component kinematically constructed using the combination of sine waves. A streamwise injection velocity $U_{in}$ is added to the kinematic velocity field, where $U_{in} = 54$ cm/s to match the statistically averaged flame burning speed predicted in the simulation. In this way, the flame does not move, on average, in the statistically stationary limit. The flow is initialized with space-filling vortices on the reactants' side of the computational domain ($x \leq 4D$).

The vortex length scale $l_v$ characterizes the concentration of vorticity in each vortex core. We define $l_v$ as the diameter of an equivalent circle with area equal to the area within the vortex that is bounded by the vorticity isocontour $0.3\omega_{peak}$, where $\omega_{peak}$ is the peak vorticity in the core. This area within the core captures more than 90% of the total vortex circulation. For the vortices of diameter $D$ defined above, it turns out that $l_v = 0.63D$. The vortex velocity scale $u_v$, characterizing the strength of the vortex core, is defined as

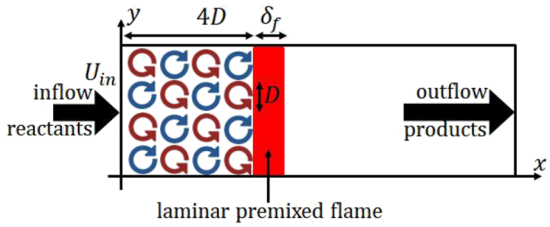


**FIG. 8.** Schematic of the computational domain for the reduced physics 2D simulation of the interactions between a flame and an array of counter-rotating vortices.


© Author(s) 2021

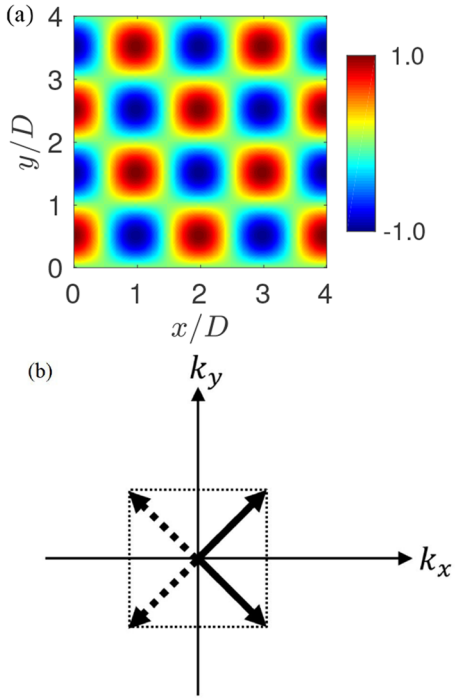


**FIG. 9.** Schematic of kinematically constructed velocity components for array of vortices injected in the inflow boundary. (a) Physical and (b) Fourier space view.

the circulation contained within the same vorticity iso-level divided by its perimeter.

The 2D flame–vortex interaction simulation was performed using the NGA code,[33] where the unsteady compressible Navier–Stokes equations under the low Mach number and ideal gas approximations and the transport equations for temperature and mass fractions of 35 species are solved with boundary conditions. The scalar equations are discretized using the BQUICK scheme, which ensures that the physical bounds of species mass fractions are numerically preserved with minimal artificial diffusion.[34] A recently developed computationally efficient, semi-implicit, iterative method is used for time-integration of the chemical source terms within the (gas-phase) species equations.[35] This method has been shown to be as computationally efficient as an explicit time-integration per time step and allows for stable simulations with larger time steps than a corresponding explicit scheme.[36]

A semi-detailed chemical kinetics model containing 35 species and 217 reactions (forward and backward reaction counted separately) is used,[37] a mechanism reduced from the original 149 species and 1651 reactions[38] to reduce the computational cost of moderate *Ka* turbulent premixed flame simulations.[37] Complete details with chemical model validation are given in Refs. 37 and 39.

The computational mesh is non-uniform in the streamwise direction and uniform in the cross-stream direction. The grid is highly refined in the vortex-dominated reaction region and, especially, in the flame region in the streamwise direction and is stretched toward the outflow boundary. At least 80 grid points are used to resolve the vortex length scale in the reactants' side and 20 grid points within the flame front thickness. A grid convergence study was carried out where we confirmed that the same results are obtained with twice as many grid points in both directions. The time step size is 1 $\mu$s to accurately resolve the chemical time scales.

### C. Coherent structure of flame–vortex interactions in physical space

The numerical simulation is analyzed selecting four primary variables associated with key features of the 2D flame–vortex interactions: the streamwise components of momentum vector ($\rho u$ and $\rho v$) as representative of momentum impacts, the mixture enthalpy ($\rho h$) containing thermal energy, and the formyl radical mass per unit volume ($\rho Y_{HCO}$) representing an intermediate species that identifies the heat release rate by combustion.[40] A single time instant within the statistically stationary state of the flame–vortex interactions is selected for analysis, when the flame is most "corrugated" as quantified by the maximum difference between the two extreme locations of the progress variable iso-level, $C = 0.5$. The statistically stationary state is observed after a transient period from the initial condition at ~4 vortex advection time scales, $D/U_{in}$.

Figure 10 shows the 2D instantaneous isocontours of primary variables, $\rho u$, $\rho v$, $\rho h$, and $\rho Y_{HCO}$, over the region of $2 \le x/D \le 8$. Taken together and as a movie, Figs. 10(a)–10(d) show the interaction between the train of vortices and laminar flame at stationary state at peak corrugation. Note from Figs. 10(a) and 10(b) that the vortices in the reactants that distort the flame are apparent in the momentum field but not in the energy or species. The interaction with the flame and baroclinic generation of vorticity at the flame leads to the development of elongated structures in the streamwise direction within the region downstream of the flame, impacted by flow acceleration and volumetric expansion within the flame front. As a consequence of baroclinic flame-generated vorticity,[41,42] the vorticity within the elongated structures is of opposite sign to the vortices on the reactants' side of the flame. It is for this reason that $\rho v$ changes sign across the flame [Fig. 10(b)].

As vortices are continuously injected into the domain from the inflow boundary, the flame is perturbed periodically in time (not shown here) and symmetrically in $y$. The train of vortices causes the formation of flame cusps when the induced velocity of two adjacent counter-rotating vortices locally advects the flame sheet into the burnt products between the vortices (at $y/D = 1$ and 3 in Fig. 10). The strength of the vortices relative to the flame sheet determines the extent to which the cusp regions extend into the products. In contrast with momentum components, $\rho h$ and $\rho Y_{HCO}$ in Fig. 10 are approximately spatially uniform on the reactants' and products' sides of the flame with large gradients localized to the thin flame. $\rho h$ has a jump from reactants to products with local scale on order the laminar flame thickness, $\delta_f$. $\rho Y_{HCO}$, by contrast, is a combustion intermediate that is highly localized with a strong peak within the reaction zone internal to the flame at a scale roughly three times smaller than the laminar flame thickness, $\delta_f$. The intermediate species generated and destroyed within the reaction zone and that contribute strongly to heat release are of this type.

From Fig. 10, four distinct coherent structural features may be identified in physical space in the primary variables: (1) vortices in momentum on the reactants' side, (2) elongated structures in momentum on the products' side (we shall refer to these


© Author(s) 2021

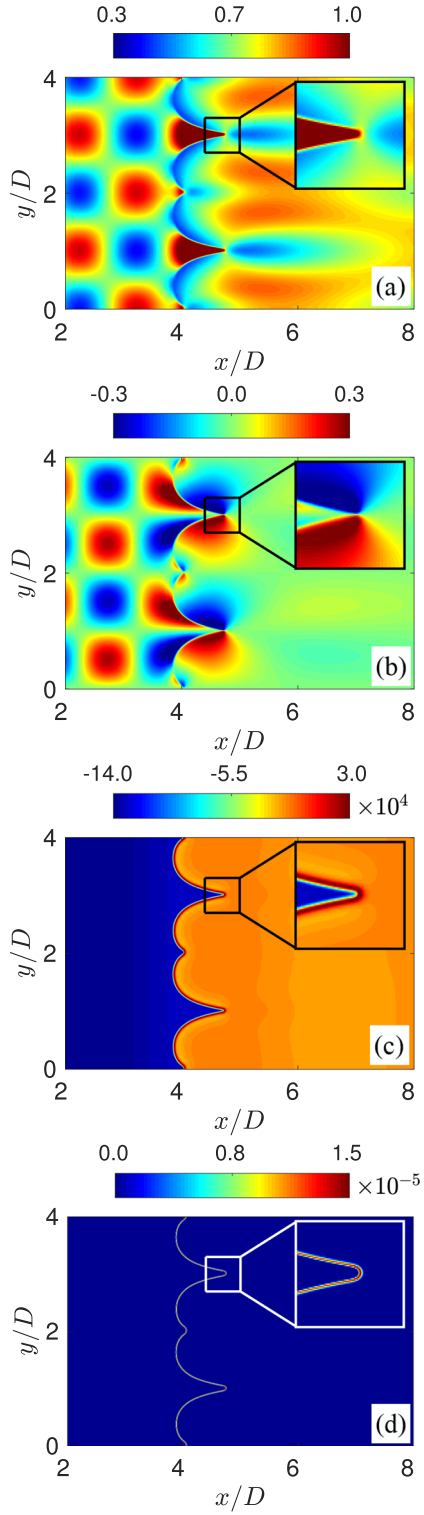


**FIG. 10.** Isocontours of primary variables in physical space for the flame–vortex interaction simulation. (a) $\rho u$ in kg/m$^2$s, (b) $\rho v$ in kg/m$^2$s, (c) $\rho h$ in J/m$^3$, and (d) $\rho Y_{HCO}$ in kg/m$^3$.

as "streaks"), (3) a corrugated flame front with locally large gradients in all variables, particularly in thermal energy and species concentration, and (4) strong streamwise jumps in energy, temperature, and some species such as fuel and oxidant (not shown) between reactants and products. In Secs. IV and V, these key physical space coherent structural features are identified with coherent features in Fourier space and are discussed in relationship to scale-decomposition within the classical LES framework.

To apply the multidimensional Fourier description to the 2D nonperiodic signals described, the nonphysical spectral content that arises from discontinuities at the boundaries in $x$ must be removed using the "discontinuity pollution removal" procedure described in Sec. II C for 1D signals but extended to 2D. In Appendix B, we describe the extension to 3D signals with one nonperiodic direction; we apply this method reduced to 2D. In Appendix C, the multidimensional procedure was validated with $\alpha = 0.85$, which ensures that the maximum signal modification remains below 5%. As a result, the vortices in the reactants ($x/D < 4$), elongated streaks in the products ($x/D > 4$), and large gradients within the flame front ($x/D \approx 4$) observed in Fig. 10 are virtually unchanged in the pollution removal periodization process (see Fig. 25 in Appendix C).

## IV. FOURIER–PHYSICAL SPACE COHERENT STRUCTURE OF FLAME–VORTEX INTERACTIONS

Figure 11 presents the concurrent Fourier space view of the physical space signals shown in Fig. 10 described in Sec. III C. In Fig. 11, we plot isocontours of the logarithmic squared Fourier coefficients for $\rho u$, $\rho h$, and $\rho Y_{HCO}$. The wavenumber axes are normalized using the laminar flame thickness, the scale defined by the boundaries of the domain in Fig. 11. The pink box identifies the vortex scale ($k_{x,y}\delta_f/\pi = \pm\delta_f/D = 0.06$) and is associated with the four Fourier modes used to construct the train of vortices that enter the computational domain (Fig. 9).

In Fourier space, the squared Fourier coefficients are symmetric due to the reality condition. An additional symmetry arises in $k_y$ because the array of symmetrical vortices creates a symmetrical response in this laminar flow. Thus, $\widehat{\phi^2}(k_x, k_y) \approx \widehat{\phi^2}(k_x, -k_y)$. The forced even spanwise symmetry in $y$ leads to negligible Fourier content in Fourier modes with wavenumber $k_y/\Delta k_y = \pm 1, \pm 3, \ldots$. To visualize better the structure, the odd $k_y$ modes are removed from all isocontour plots. We refer to "Fourier energy content" as the squared Fourier coefficients, which represent wavenumber-specific contributions to variance. To better understand how coherent structure (described in Sec. III C) is characterized in Fourier space, systematic spectral filtering is applied.

### A. Analysis of small-scale structure

For the primary variables shown in Fig. 11, the highest magnitude Fourier energy content is found to be organized within a star-like pattern toward high wavenumbers (i.e., small scales) that extend from the vortex to flame scale. The $\rho Y_{HCO}$ energetic Fourier content extends to $k_{x,y}\delta_f/\pi \approx \pm 3$ (not shown here), the reaction zone scale within the premixed flame.


© Author(s) 2021

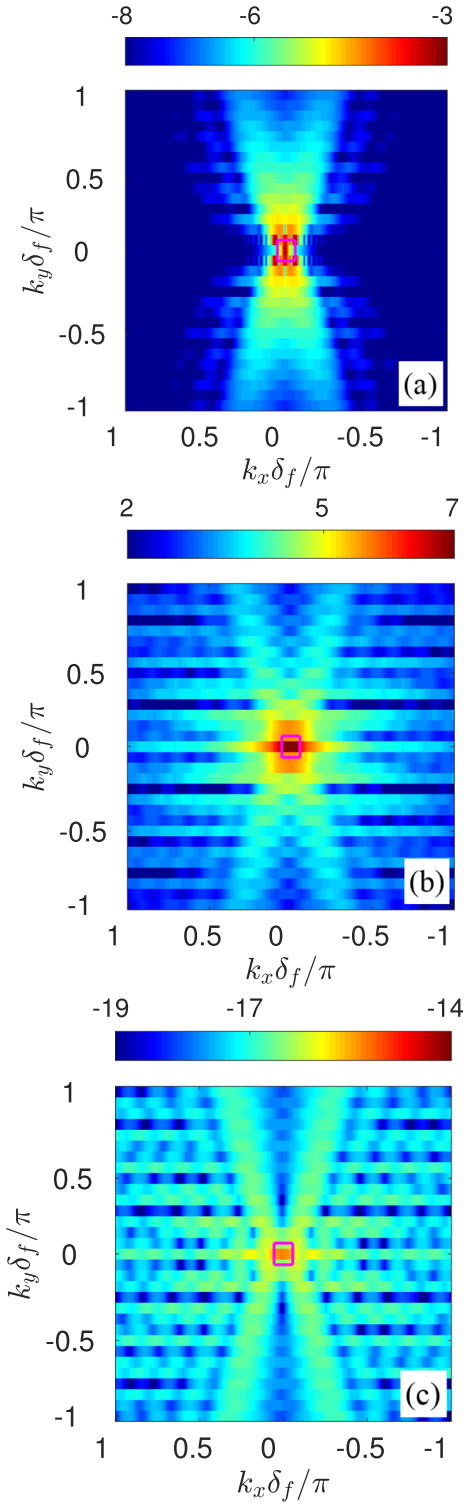


**FIG. 11.** Isocontours of the logarithmic squared Fourier coefficients of the same primary variables at the same time instant in the flame–vortex interaction as Fig. 10. The pink box identifies the vortex scale ($k_{x,y}\delta_f/\pi = \pm\delta_f/D = 0.06$). (a) $\log_{10}(\widehat{\rho u^2})$, (b) $\log_{10}(\widehat{\rho h^2})$, and (c) $\log_{10}(\widehat{\rho Y_{HCO}{}^2})$.

To identify the physical space content associated with the correlated collections of Fourier modes within the legs of the star-like pattern in the 2D spectral content in Fig. 11, we designed localized elliptical filters (conceptually bandpass-like) that we optimally aligned with the legs of the star patterns and their symmetric counterpart. The two characteristic scales of the ellipse in 2D Fourier space were estimated qualitatively. In Fig. 12, we show the filtered signals above and the unfiltered signals below for momentum, energy, and species concentraion variables shown in Figs. 10 and 11. Whereas the filter is designed to capture the four dominant legs in the star-like pattern, the wavenumbers within the vortex-scale box ($|k_{x,y}|\delta_f/\pi \leq 0.06$) are not captured by the filter. Indeed, the legs of the star-like pattern extend from the vortex scale box to, and beyond, the flame scale box.

Figure 13 shows in physical space the filtered and original signals in the top and bottom halves of each isocontour, respectively. The mean value of the variable was removed by the filter, so the mean values are added to the filtered signals in Fig. 13 for direct comparison with the original physical space signals. We observe that the star-like region of Fourier space corresponds to physical space structures that surround and define the corrugated flame front. The smaller scale features of the flame front in the insets of Fig. 10 are captured by the coherent star-like regions of Fourier space identified in the insets of Fig. 13. In particular, these regions of Fourier space appear to recover most of the flame cusps in $\rho u$. However, not all the corrugations of the flame are recovered, as observed by the sharp angles between segments of filtered $\rho Y_{HCO}$ in Fig. 13(c) compared with the smooth large-scale segments in the original signal.

As discussed in Sec. II, the Fourier variance content of a discontinuity has power-law decay to the grid cutoff scale. The star-like patterns in Fourier space are, in reality, power-law decays arising from near-discontinuities at the flame front. Given the finite thickness of the flame front and the sharp, but smooth, variation across the front, the Fourier energy content exhibits power-law decay down to the flame front scale. At the flame thickness, the Fourier variance transitions to exponential decay (to the grid cutoff scale). The directions of the "star legs" are normal to the corresponding sections of flame front that generates the power-law decay.

To better understand the connection between the star-like pattern in Fourier space and the corrugated flame front in physical space, we compute the flame-normal gradient of primary variables along the flame centerline (progress variable iso-level, $C = 0.5$). The unit normal vector direction is defined as $\vec{n} = -\nabla T/|\nabla T|$ and indicated as $\vec{n}_f$ at the flame centerline.

Figure 14 shows the position of the flame centerline iso-level in the $(x, y)$ plane colored according to the magnitude of the local flame-normal gradient of each variable multiplied by the laminar flame thickness, which provides an estimate of the local "jump" across the flame. We note that the normal gradients are highly localized to the flame sheet and that whereas the magnitude of the local normal gradient is relatively uniform along the sheet with $\rho h$ and $\rho Y_{HCO}$ concentration, this is not the case with momentum, which shows large variability along the sheet.

Figure 15 shows the Probability Density Function (PDF) of the angle $\theta_f$ between the flame centerline direction $\vec{n}_f$ and the streamwise direction, $x$ (counterclockwise direction). This PDF is approximately symmetric, as the flame corrugations are caused by a symmetric array of vortices along the cross-stream direction. Four


© Author(s) 2021

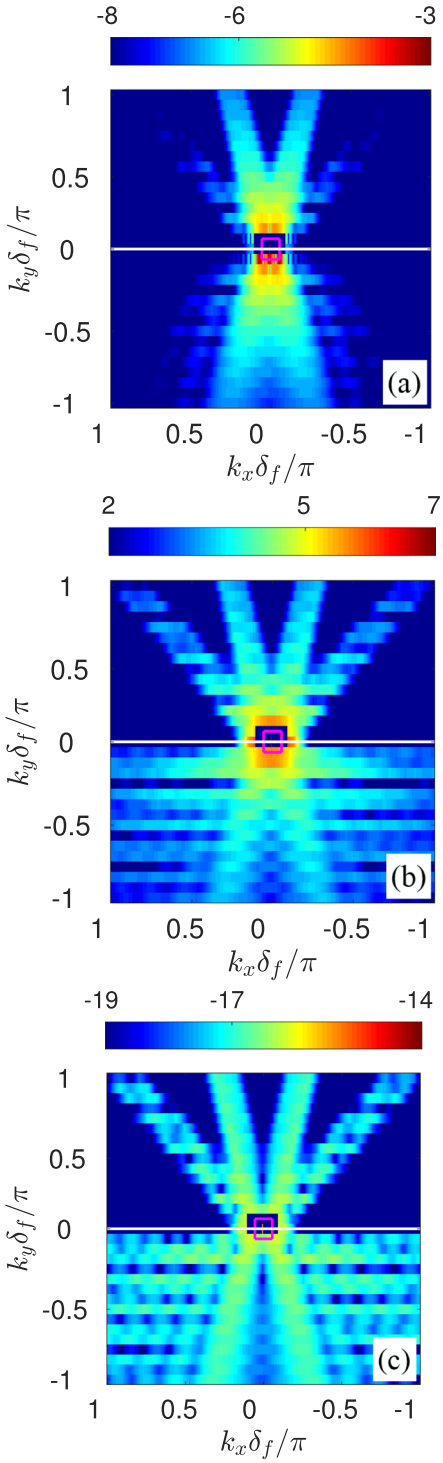


**FIG. 12.** Isocontours of the logarithmic squared Fourier coefficients of primary variables shown in Fig. 11. The filtered and original signals are shown in the top and bottom halves of each figure, respectively. As discussed in the text, the filter is constructed to extract Fourier content within the star-like pattern in Fourier space and the pink box identifies the vortex scale ($k_{x,y}\delta_f/\pi = \pm 0.06$). (a) $\log_{10}(\widehat{\rho u^2})$, (b) $\log_{10}(\widehat{\rho h^2})$, and (c) $\log_{10}(\widehat{\rho Y_{HCO}{}^2})$.

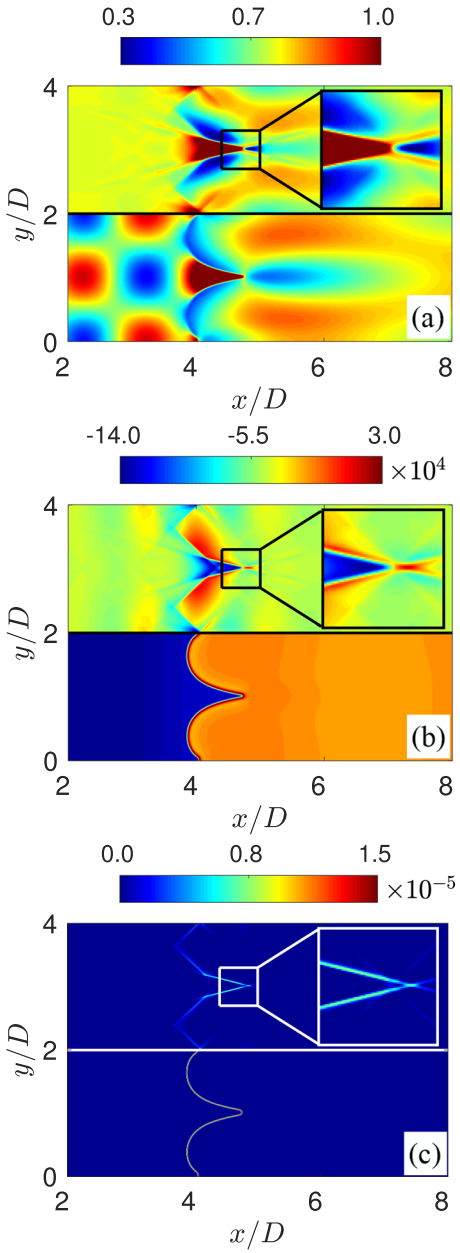


**FIG. 13.** Isocontours of primary variables in physical space shown in Fig. 10. The filtered and original signals are shown in the top and bottom halves of each isocontour, respectively. As discussed in text, a filter is constructed to extract Fourier content within the star-like pattern in Fig. 12. The insets show the filtered signal at the flame cusps. (a) $\rho u$, (b) $\rho h$, and (c) $\rho Y_{HCO}$.

dominant peaks around ±45° and ±75° may be identified, which match the angles of dominant legs in the star-like pattern observed in Fig. 12. The dominant peaks in the PDF at $\theta_f \approx \pm 75°$ are associated with the more pinched flame cusps ($y/D = 1$ and 3 in Fig. 13), which cover a large segment of the flame centerline, and the secondary


© Author(s) 2021

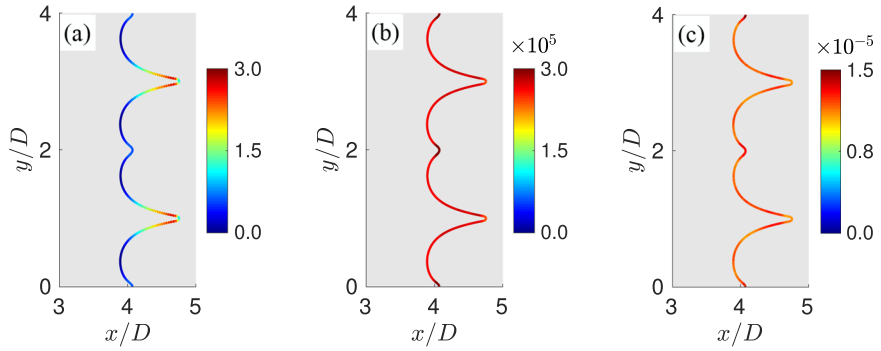


**FIG. 14.** Magnitudes of flame-normal gradients (a) $\delta_f|\vec{n}_f \cdot \nabla(\rho u)|$ (kg/m$^2$s), (b) $\delta_f|\vec{n}_f \cdot \nabla(d\rho h)|$ (J/m$^3$), and (c) $\delta_f|\vec{n}_f \cdot \nabla(\rho Y_{HCO})|$ (kg/m$^3$) over the flame centerline defined by the progress variable iso-level, $C = 0.5$.

peaks at $\theta_f \approx \pm 45°$ represent the smaller flame cusps ($y/D = 0$, 2, and 4 in Fig. 13).

The larger magnitude of the flame-normal jump of $\rho u$ over the more pinched flame cusps [Fig. 14(a)] produces the Fourier content dominantly along the legs oriented at ±75° [Fig. 12(a)]. In contrast, both thermochemical variables are shown to have approximately uniform flame-normal jump over the flame centerline [Figs. 14(b) and 14(c)], as the internal flame structure is preserved during the relatively weak ($u_v/s_L \approx 0.5$) flame–vortex interactions.

The variability in the magnitude of the flame-normal jump along the flame centerline is quantified by its intensity (standard deviation divided by mean). The intensities of $\rho u$, $\rho h$, and $\rho Y_{HCO}$ are 84%, 6.8%, and 9.1%, respectively. Thus, the star-like pattern of $\rho h$ and $\rho Y_{HCO}$ is approximately insensitive to the magnitude of flame-normal jump and is dictated by the PDF of $\theta_f$. Therefore, dominant legs in the star-like pattern of $\rho h$ and $\rho Y_{HCO}$ are observed at ±75°, secondary legs are observed at ±45°, and non-negligible content is observed over a broad range of angles [Figs. 11(b) and 11(c)].

The analysis of this section indicates that physical space coherent structure associated with the corrugated flame front creates organization (coherence) in Fourier space, which, at the smaller scales, corresponds to a star-like pattern with significant Fourier energy content extending from the vortex scale box to the flame scale and smaller (Figs. 12 and 13). From the perspective of typical LES scale decomposition, this physical–Fourier space duality in the coherent structure would be partially resolved by the grid and dynamics and partially subfilter scale. The understanding of dynamically coherent structure could be impactful to dynamically relevant SFS modeling. In Sec. IV B, we define RS consistent with the LES framework to facilitate identification and quantification of coherent structure in the physical–Fourier space duality at the RS and SFS consistent with classical LES.

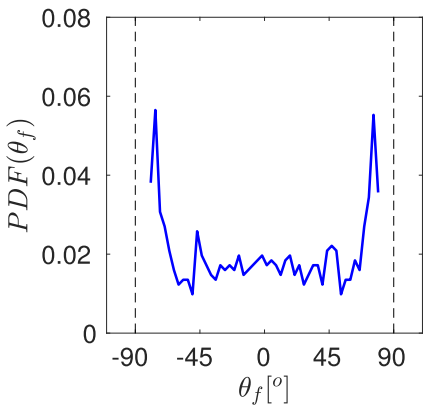


**FIG. 15.** PDF of the local flame centerline angle $\theta_f$ between the flame centerline direction $\vec{n}_f$ and the streamwise direction (counterclockwise direction).

## B. Defining resolved vs subfilter scales consistent with LES

In the classical LES framework, resolved fluctuations defined by the effective grid are carried forward in time in the numerical simulation, where "effective" implies the additional coarsening of the geometric grid due to the impacts of the numerical and model dissipation. A geometric grid properly designed for LES is the one in which the corresponding effective grid resolves a large percentage of variance of fluctuations in momentum and energy where "large" implies capturing covariances at the 80%–90% level. As discussed below, here we require at least 85% of the resolved variance of momentum ($\rho\vec{u}$) and enthalpy ($\rho h$) per unit volume. The variance is calculated after removing two-dimensional averaged values, equivalent to the sum of squared Fourier coefficients excluding $\vec{k} = 0$.

We define "resolved scales" using a 2D sharp low-pass rectangular "effective grid" filter in Fourier space with wavenumber cutoffs $k_{G,x}$ and $k_{G,y}$. We define the single characteristic filter wavenumber scale as $k_G \equiv \sqrt{k_{G,x}k_{G,y}}$. The optimal wavenumber cutoffs $(k_{G,x}, k_{G,y})$ that define the RS wavenumber cutoffs are obtained performing parametric variations to minimize $k_G$ with specified fixed percentage of total captured variance over the statistically stationary regime of the simulation. Figure 16 presents 2D isocontours of $k_G$ over the $k_{G,x} - k_{G,y}$ parameter space nondimensionalized by the laminar flame thickness. The colored iso-lines in Fig. 16 indicate wavenumber cutoffs $(k_{G,x}, k_{G,y})$ that capture *at least* 70%, 80%, 85%, and 90% of the total variance for $\rho u$, $\rho v$, and $\rho h$. The solid circles identify the corresponding optimal wavenumber cutoffs based on minimum $k_G$ for each iso-line, which provides the respective wavenumbers $k_{RS,x}$ and $k_{RS,y}$ that define the rectangular RS region in 2D Fourier space.

Figure 16 indicates that the RS wavenumber cutoffs are systematically asymmetric $k_{RS,y} > k_{RS,x}$. This is due to the cross-stream corrugations of the flame front with content at higher $k_y$. The observation that the colored iso-lines in Fig. 16 become approximately vertical and horizontal at higher $k_{G,y}$ and $k_{G,x}$ reflects the rapid drop


© Author(s) 2021

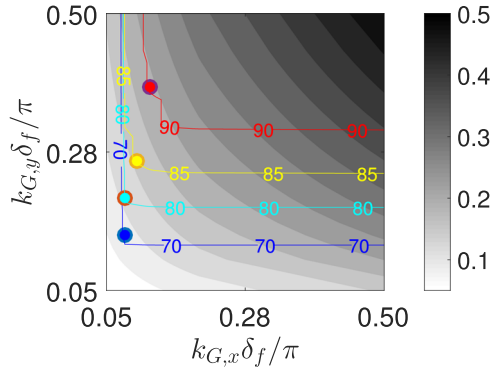


**FIG. 16.** Isocontours of nondimensional filter wavenumber cutoff $k_G\delta_f/\pi$ over the $k_{G,x} - k_{G,y}$ parameter space. The colored iso-lines indicate the percentage variance content captured by the filter relative to the energy content of the original signal. The solid circles indicate the minimum $k_G$ at the given percentage variance content level.

in variance that occurs as the filter cutoff crosses the wavenumbers associated with the vortices, $k_{G,(x,y)}\delta_f/\pi = 0.06$, which contain a large percent of momentum variance. The $\rho h$ variance is largely contained in first few wavenumbers in 2D Fourier space [Fig. 11(b)], so the colored iso-lines shown in Fig. 16 solely depend on the captured momentum variance. The conclusions from this study were found to be qualitatively insensitive to the choice for percentage variance in RS fluctuations between ~80% and 90%. We therefore chose *at least* 85% variance in momentum and enthalpy per unit volume to define "resolved scales." The resulting wavenumber cutoffs are $k_{RS,x}\delta_f/\pi = 0.1$ and $k_{RS,y}\delta_f/\pi = 0.26$ (yellow symbol in Fig. 16). This corresponds to the smallest resolved lengths scale in the streamwise and cross-stream directions $\ell_{RS,x} = \pi/k_{RS,x} = 0.62D$ and $\ell_{RS,y} = \pi/k_{RS,y} = 0.24D$, respectively.

The procedure described above does not include the variance content of $\rho Y_{HCO}$, which as previously discussed characterizes heat release in the reaction zone that is generally unresolved in practical LES. In the current analysis, for example, the wavenumber cutoffs would increase to $k_{G,x}\delta_f/\pi = k_{G,y}\delta_f/\pi = 3$ to capture 85% of the variance of $\rho Y_{HCO}$, which would result in $\rho u$ and $\rho h$ being nearly fully resolved by the effective grid. In this case, the simulation would be close to a DNS. We conclude that not all dynamical equations for turbulent reacting flows can be treated within the classical LES framework and SFS modeling strategies. This is because key chemistry-related dynamics necessarily takes place at scales associated with molecular diffusion, which is not resolvable in practical LES, invalidating the key LES assumption that all dominant dynamics is captured by the effective grid and that the models for SFS terms must primarily capture forward-cascade dynamics.

### C. Analysis of resolved-scale structure

We continue our analysis within the LES framework using the effective grid filter described in Sec. IV B. Figure 17 shows in physical space the RS and original signals in the top and bottom halves of each isocontour plot, respectively. In Fig. 17, we show the RS flame front with boundaries defined by isocontour levels 0.05 and 0.85 of the resolved temperature-based progress variable $C^r = (T^r - T^r_u)/(T^r_b - T^r_u)$, where the superscript $r$ indicates the RS

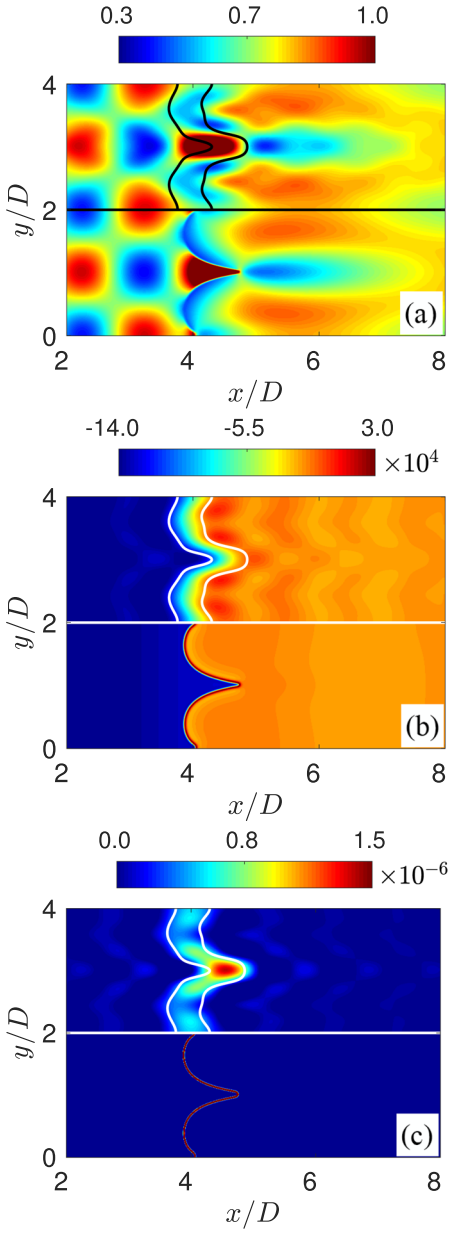


**FIG. 17.** Isocontours of primary variables in physical space. The resolved and original signals are shown in the top and bottom halves of each isocontour plot, respectively. (a) $\rho u$ in kg/m$^2$s, (b) $\rho h$ in J/m$^3$, and (c) $\rho Y_{HCO}$ in kg/m$^3$.

variable. Figure 17 indicates that the large-scale structural features of key variables are readily identified in the full field (bottom halves of each isocontour). These include the vortices in the reactants' side and the elongated streaks on the products' side for $\rho u$ [Fig. 17(a)]. The RS corrugated flame front is less corrugated and thicker, with corresponding lower flame-normal gradients within the front, than the full field, which contains the small-scale features that exist within the SFS motions.


© Author(s) 2021

Figures 12 and 13 describe coherent Fourier and physical space features at the flame front, which are associated with the star-like pattern that extends from the low wavenumber vortex scales (magenta box in Figs. 12 and 13) to the high wavenumbers at the flame and reaction zone scales (beyond the domain boundaries in Figs. 12 and 13). However, accurate LES requires accurate prediction of RS dynamics. Thus, the relationships between RS coherent structures in Fourier vs physical space are of primary interest. Figure 18 presents the concurrent view in Fourier space of the RS signals shown in the top halves of Fig. 17, where isocontours of the logarithmic squared Fourier coefficients for each primary variable are shown within the Fourier space rectangle defined by our determined RS wavenumber cutoffs ($|k_x|\delta_f/\pi \le 0.1$ and $|k_y|\delta_f/\pi \le 0.26$). The color bars of Fig. 18 span the same range as in Fig. 12, and the magenta lines correspondingly indicate the vortex-scale box ($k_{x,y}\delta_f/\pi = \pm\delta_f/D = \pm 0.06$). SFS modes are identified by the white regions in Fig. 18. In contrast to the star-like pattern discussed in Sec. IV A, which covers a wide broadband range of mostly SFS fluctuations, the Fourier content toward low wavenumbers (i.e., larger RS motions) is shown to be localized over a reduced number of Fourier modes, such as the four corners of the vortex scale box in $\rho u$ in Fig. 18(a).

By systematically filtering such spectral regions of interest within the RS rectangle in Fig. 18 using localized rectangular sharp filters, we have identified four distinct regions in Fourier space in Fig. 19 that characterize distinct features of the resolved scales. We systematically compute the inverse Fourier transform of the filtered Fourier coefficients within the four sub-regions identified in Fig. 19 and analyze the corresponding physical space structure. The distinct colored subregions in Fig. 19 represent the 2D sharp Fourier space filters employed to decompose the resolved scales.

### 1. Vortices

Figure 18(a) shows the high magnitude Fourier content at and near the corners of the vortex-scale box for $\rho u$. The four corners are, by construction, the modes used to generate the single-scale vortices injected into the flow through the Dirichlet boundary conditions at the inflow boundary (Fig. 9). The Fourier coefficients surrounding these forcing modes are isolated using the 2D sharp Fourier space filter identified by the blue regions of Fig. 19, which filters Fourier modes in the spectral areas $|k_y|\delta_f/\pi = 0.06$ and $0.05 < |k_x|\delta_f/\pi \le k_{RS,x}\delta_f/\pi$. Figure 20 shows the physical space view of the sub-filtered field associated with RS vortices above in comparison with the complete RS field below. The filtered $\rho u$ field characterizes the vortices on the reactants' side of the mixture, effectively matching the complete RS signal up to $x \lesssim 3.5D$. If only the four Fourier coefficients associated with the corners of the vortex-scale box were extracted, the filtered physical space signal would describe vortices spread uniformly over the entire computational domain. The additional Fourier modes and their phase relationships suppress the signal associated with the vortices on the products' side of the flame, localizing the vortices in the flame–vortex interactions to the reactants' side of the mixture.

### 2. Elongated streaks

The high magnitude RS Fourier content observed for $\rho u$ in Fig. 18(a) and identified by the green regions in Fig. 19 at $k_x$ surrounding zero and $k_y\delta_f/\pi = \pm 0.06$ is associated with the physical space structure that has characteristic length scales in the streamwise direction $x$, which are larger than the vortex scales in $y$ where $k_y\delta_f/\pi$ is that for vortices created to force the flame. The Fourier coefficients isolated using the 2D sharp Fourier space filter over the green region in Fig. 19 are located at $|k_y|\delta_f/\pi = 0.06$ and within $|k_x|\delta_f/\pi \le 0.05$.

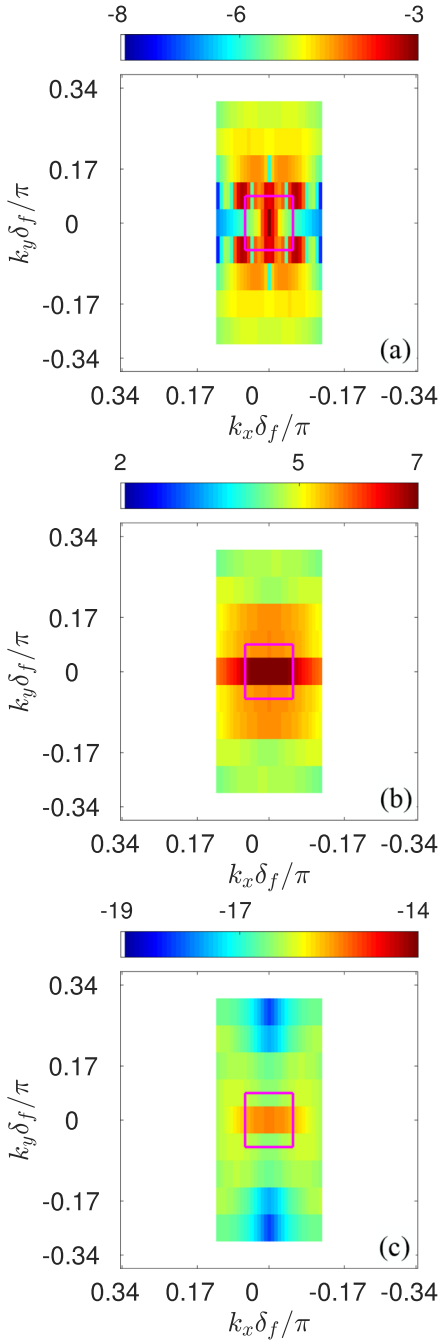


**FIG. 18.** Isocontours of the logarithmic squared Fourier coefficients of primary variables at the resolved scales. SFS modes are in the white. (a) $\log_{10}(\widehat{\rho u^2})$, (b) $\log_{10}(\widehat{\rho h^2})$, and (c) $\log_{10}(\widehat{\rho Y_{HCO}{}^2})$.


© Author(s) 2021

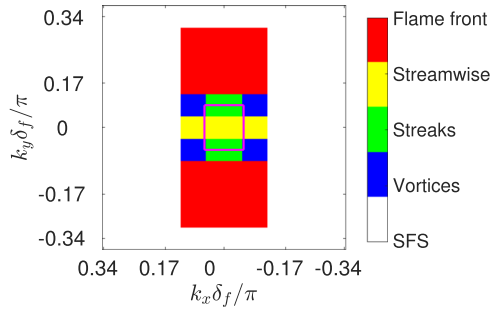


**FIG. 19.** Four distinct color-coded RS sub-regions in Fourier space.

Figure 21 compares the inverse FTF of the sub-filtered $\rho u$ field above with the complete RS field below. The sub-filtered RS field characterizes the elongated streaks in the burned products' side of the mixture. The degree of localization of the filtered physical space signal toward the burnt products' side is a result of the phase correlations among the Fourier coefficients within the green sub-filtered region in Fig. 19. The relationship between the Fourier coefficients associated with vortices and elongated streaks is controlled by the dynamical interaction between the vortices and flame kinetics to create elongated streaks due to volumetric expansion as the vortices interact with the flame front.

### 3. Corrugated flame front

As discussed in Sec. IV A, the physical space coherent structure associated with the highest gradients associated with the reaction zone in the corrugated flame front is organized in Fourier space within a star-like pattern that extends from the vortex scale box to beyond the flame scale box (Fig. 12), which is from the smallest SFS motions to within the RS motions. Thus, in an LES, the physical space structure associated with these Fourier coefficients are partially resolved scale and partially subfilter scale. The RS content of the corrugated flame is characterized by the Fourier modes within the red spectral "flame front" region in Fig. 19, the region $0.06 \le |k_y|\delta_f/\pi \le k_{RS,y}\delta_f/\pi$ and $|k_x| \le k_{RS,x}$. The sub-filtered physical space counterpart of these sub-filtered Fourier coefficients is presented in Fig. 22 for primary variables of interest in the upper half of each figure for comparison with their respective complete RS signals in the lower half of each figure. Figure 22 shows that the sub-filtered signals characterize, in physical space, the RS flame cusp associated with the RS flame front corrugations in the cross-stream direction. The black lines in Fig. 22 indicate progress variable values 0.05 and 0.85 in the RS temperature field. The variance associated with these Fourier coefficients makes the RS wavenumber cutoffs systematically non-isotropic ($k_{RS,y} > k_{RS,x}$, in Sec. IV B), consistent with the RS structure of the large-scale cross-stream corrugations in the flame front. Therefore, the largest scale content of the star-like pattern described in Sec. IV A (Fig. 12) is resolved by the LES effective grid, with the higher gradient small-scale features of the corrugated flame mostly subfilter scale.

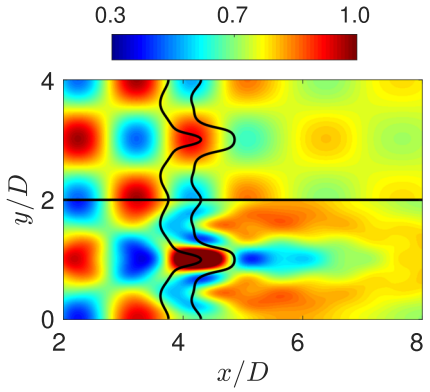


**FIG. 20.** We show the physical space view of the sub-filtered field associated with the RS vortices (blue subregions of Fig. 19) in comparison with the complete RS field shown below for $\rho u$ (kg/m$^2$s).

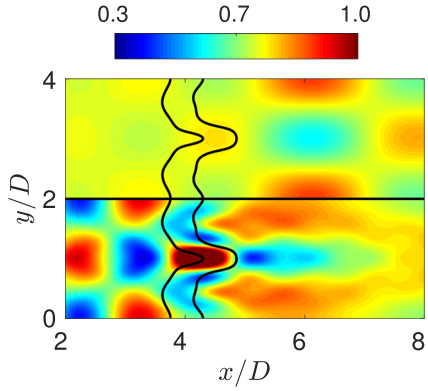


**FIG. 21.** We show the physical space view of the sub-filtered field associated with the RS elongated streaks (green subregions of Fig. 19) in comparison with the complete RS field shown below for $\rho u$ (kg/m$^2$s).

### 4. Streamwise front

The final physical/Fourier space coherent structure identified is associated with the cross-stream averaged gradients in the corrugated flame front, referred to as "streamwise front" in Fig. 19, characterized by the Fourier modes within the yellow spectral sub-region, the region $k_y = 0$ and $|k_x| \le k_{RS,x}$. Figure 23 shows the physical space view of the sub-filtered field associated with streamwise gradients in the flame front in comparison with the complete RS field (below). In particular, the streamwise flame front reflects the jump of $\rho h$ from reactants to products and the localized concentration of $\rho Y_{HCO}$ within the flame front, as described in Sec. III C.

## D. Energy content in distinct structures

The systematic filtering operations described in Sec. IV C relate the coherent structure in physical space to the coherent structure in Fourier space in context with LES of premixed turbulent combustion. To quantify the relative variance content of the distinct physical/Fourier space coherent structures for primary variables of interest, we compute the filtered variance content of each coherent structure as the sum of squared Fourier coefficients over the sub-regions in RS Fourier space shown in Fig. 19. We have found that these characterize distinct structural features in physical space. Figure 24 presents for each variable the percentage of variance contained in each coherent structure relative to the energy contained in the total original signal.


© Author(s) 2021

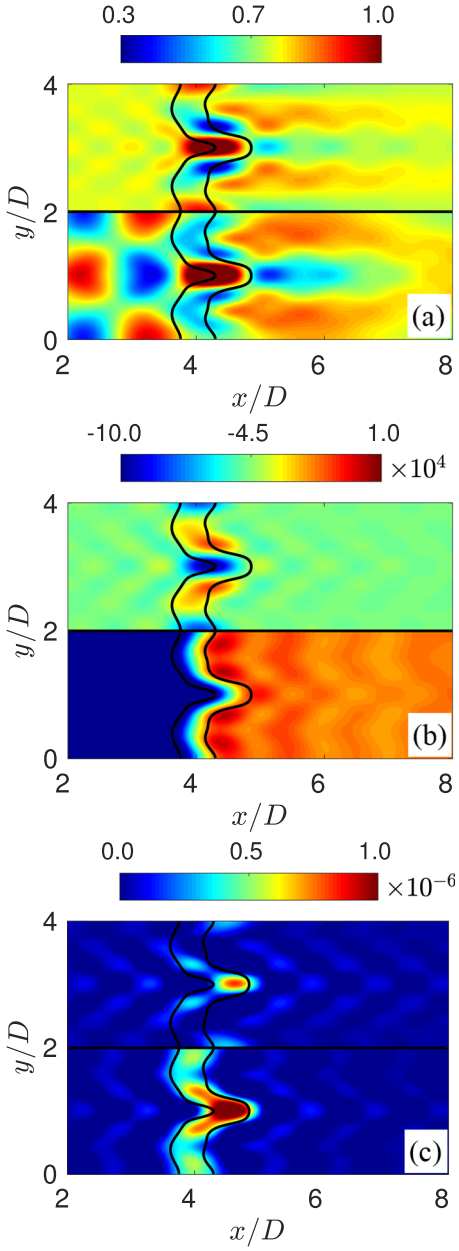


**FIG. 22.** We show the physical space view of the sub-filtered field associated with the RS corrugated flame front (red subregions of Fig. 19) in comparison with the complete RS field shown below for (a) $\rho u$ (kg/m$^2$s), (b) $\rho h$ (J/m$^3$), and (c) $\rho Y_{HCO}$ (kg/m$^3$).

The sum of the color bars in Fig. 24 gives the total % variance resolved by the effective grid. We note that the momentum and enthalpy are resolved, by construction, at least at the 85% level. The variance of $\rho Y_{HCO}$, on the other hand, is only 8% resolved. Created and destroyed in the reaction zone, HCO as of several important species with dynamics underlying heat release largely unresolved

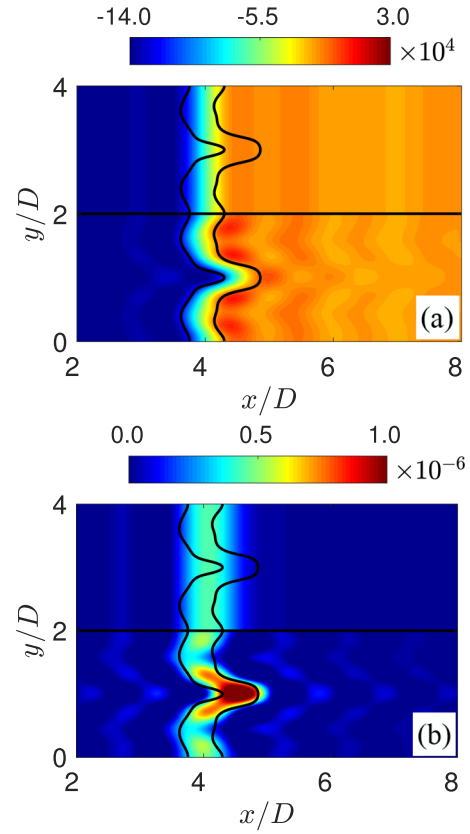


**FIG. 23.** We show the physical space view of the sub-filtered field associated with the RS streamwise front (yellow subregions of Fig. 19) in comparison with the complete RS field shown below for (a) $\rho h$ (J/m$^3$) and (b) $\rho Y_{HCO}$ (kg/m$^3$).

by practical LES. As discussed in Sec. IV A, the star-like pattern is associated with reaction zone kinetics. This narrow frontal structure exists within the corrugated RS flame front described in Sec. IV C and is the dominant SFS coherent structure.

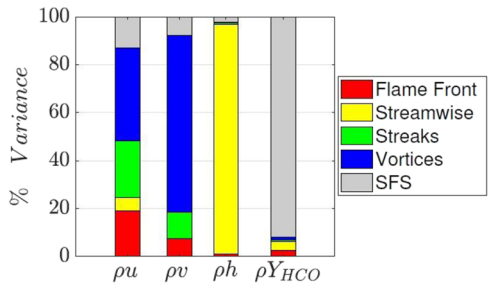


**FIG. 24.** Percent variance content in $\rho u$, $\rho h$, and $\rho Y_{HCO}$ in the RS flame front (red), RS streamwise front (yellow), RS elongated streaks (green), RS vortices (blue), and SFS motions (gray) for the flame–vortex interaction simulation. The percent variance is relative to the total variance of the complete (RS and SFS) signal.


© Author(s) 2021

Figure 24 indicates that the RS variance of $\rho u$ is dominated by the vortices, elongated streaks, and RS corrugated flame with relatively small contribution from the streamwise front. In contrast, the RS variance of $\rho h$ is fully dominated by the streamwise front and the dominantly SFS variance of the species $\rho Y_{HCO}$ is associated with the internal reaction zone where heat release is highly localized. These results suggest that in a turbulent premixed flame RS momentum evolution contains a major contribution from the RS flame front. Since in Fourier space the corrugated flame front is a coherent structure that resides in both the resolved and subfilter scales, dominant inter-scale couplings in the evolution of RS momentum occur within the multiscale coherent structure associated with the flame front.

The modeling of inter-scale couplings is more critical for the combustion intermediates that are directly involved in heat release, such as $\rho Y_{HCO}$, where the variance content is largely at the subfilter scales. The turbulent combustion dynamical system therefore makes it difficult to maintain the classical LES framework in which the geometrical and effective grids are designed to resolve a large percentage of the variance of all dynamically relevant variables with the impacts of RS–SFS interaction on RS evolution well approximated by models that characterize statistically a dominantly forward-cascading interscale dynamics.

## V. DISCUSSION AND CONCLUSIONS

The current study has two interrelated motivations: (1) the development of a "discontinuity pollution removal" procedure that removes nonphysical Fourier content arising from boundary discontinuities when the FTF of a bounded analytic signal is taken in a nonperiodic direction, without significantly modifying the signal away from the boundaries (Sec. II and Appendix B) and (2) analysis of the relationship between the same coherent structure in physical space and in Fourier space with data from a reduced physics simulation designed to have key characteristics of flame–turbulence interactions that are characteristic of flame–turbulence interactions in premixed turbulent combustion (Sec. IV). Because discontinuity pollution removal is required preceding our analysis of the coherent structure in Fourier space, we use this simulation also to validate the pollution-removal method (Appendix C).

Our discontinuity pollution removal procedure has potential applications that extend well beyond multidimensional Fourier analysis of premixed turbulent combustion DNS, where "discontinuity" is, in reality, a large gradient with magnitude determined by the fixed boundary jump and the resolution of the grid. Based on the mathematical identification of the specific Fourier content associated with the nonperiodicity of the signal (Sec. II B), it is both a "pollution removal" and a (partial) signal periodization procedure. "Partial" periodization arises from the tradeoff between (i) the removal of spectral content associated with the nonphysical discontinuity that is created at the boundaries by the bounded Fourier transform of nonperiodic signals and (ii) the degree of alteration of the original signal away from the boundaries. Fully periodizing a signal with our approach requires the subtraction from the original signal of all spectral content of a "discontinuity function" that contains the same boundary discontinuity as in the original signal as well as a linear ramp between the boundaries, which impacts the signal everywhere.[23,25] To avoid this problem, discontinuity removal is confined to high wavenumbers above a user-determined high-pass filter cutoff that localizes the modification of the signal to the boundary discontinuity, thus minimizing changes to the signal away from the boundary. However, application of the high-pass filter leaves behind a residual level of boundary discontinuity with the associated residual level of nonperiodicity. We designed a procedure that determines an optimal high-pass filter cutoff as a function of a user-chosen parameter that decides the degree of residual boundary discontinuity (and nonperiodization) vs the level of modification of the original signal away from the boundaries (Sec. II C). Whereas in Sec. II the discontinuity pollution removal procedure is developed for analytic 1D signals, the approach is extended to 3D signals with one nonperiodic direction in Appendix B. Our approach is useful to other applications where the spectral analysis of nonperiodic computational or experimental signals is required, and we expect that our approach can be generalized and improved.

We developed a detailed analysis to study and validate our approach using 2D data from a flame–vortex–train interaction simulation in Appendix C. In the course of the validation analysis, we learn that the optimization process to determine the filter cutoff wavenumber, together with the choice of the user-defined parameter $\alpha$, retains the large-scale unadulterated content while removing the polluting influence of the boundary discontinuity. This process uncovers the true diffusion-induced exponential spectral drop-off at higher wavenumbers, which was fully masked by the power-law content of Fourier modes created by the unphysical boundary discontinuity. It now becomes possible to analyze the true multidimensional spectral content of nonperiodic signals. This is necessary for our application to the calculation of the nonlinear triadic (and quadratic) interactions underlying essential nonlinearities, the subject of a future submittal (briefly summarized in the work of Paes *et al.*[10]).

Having removed signal pollution in the nonperiodic direction, we analyzed the relationships between coherent structures in physical and Fourier space through the application of systematic localized filtering in Fourier space in context with the multidimensional Fourier representation of scale content (Sec. IV). Collections of Fourier coefficients are shown to be connected to localized coherent structures in physical space, where "coherence" is embedded in the phase correlations that exist among individual Fourier coefficients at different scales in different directions (i.e., positions in Fourier space) underlying the physical space representation of the coherent structure.

In particular, a small-scale coherent structure is organized within a coherent broadband "star-like" pattern in Fourier space that extends from the vortex to the flame scales (Sec. IV A). The magnitudes and directional dependences of the Fourier coefficients within the legs of the star are shown to be closely connected with the direction and magnitude of flame-normal gradients of key variables within the corrugated flame front. This observation suggests that the Fourier content of flame–turbulence interactions would also be organized in the coherent broadband star-like pattern over a wide range of angles due to the wide range of flame corrugations caused by turbulence. The current study shows that, in more complex multiscale turbulence–flame interactions, collections of flame segments with similar flame-normal orientation may be isolated by the systematic application of specific filtering operations in Fourier space developed in the current study. With this understanding, it is


© Author(s) 2021

possible to analyze DNS studies to relate embedded coherence in multidimensional scale space to specific nonlinear interactions underling evolution in physical space.[10]

For a consistent interpretation of our reduced-physics simulations in relationship to LES, we defined resolved scales with a 2D Fourier space filter that decomposes the scale-based content of fluctuations in key variables into "resolved" vs"subfilter" scales (RS vs SFS) based on the key criterion underlying LES that the spectral content of the variances of key variables is captured by the effective grid to the 80%–90% level (Sec. IV B). The LES framework includes the requirement that, statistically, nonlinear interscale interactions transfer information from the larger resolved scales to the smaller, and much less energetic, subfilter scales. In this way, RS evolution is impacted only indirectly by SFS fluctuations. Both of these requirements are necessarily violated in LES of premixed turbulent combustion due to the critical existence of key kinetics that lead to heat release at scales unresolvable by the grid. Consequently, the range of resolved scales is defined based on the relative RS variance of momentum and thermal energy fluctuations, but not on species concentrations.

Interestingly, our analysis shows the direct correspondence between localized regions of RS Fourier space and coherent structural features in physical space at the resolved scales, implying that it is now possible to isolate the interscale couplings underlying the evolution of specific structural features. Most importantly, we have identified the localized regions in 2D Fourier space, which correspond to the corrugations in the flame front in the transverse direction in response to forcing by the vortex train, as well as axial gradients associated with the overall planar structure of the flame. In addition, we have shown that the elongated structures within the products that are created as eddies pass through the flame are localized in Fourier space to axial wavenumbers near $k_x = 0$ and spanwise wavenumbers that match the dominant spanwise wavenumbers $k_y$ of the forcing eddies. We anticipate that these general groupings of Fourier modes exist in fully turbulent flame–turbulence interactions with details dependent on the scales and strengths of the turbulence eddies that distort the flame front, making it possible to study nonlinear scale interactions associated with specific features underlying flame–turbulence dynamics in premixed turbulent combustion. The relative variance content of different coherent structures provides the kinematic significance of distinct structural features for the key variables and their relative RS vs SFS content in LES (Sec. IV D). Whereas over 90% of the variance of HCO is subfilter scale, momentum fluctuations are mostly resolved by the effective grid. Although major fluctuations in momentum may be found in the vortices on the reactants' side and streaks on the products' side of the flame (i.e., the turbulence eddies), significant variance content also exists in the deformations of the flame front (Fig. 24).

In Sec. IV A, we explained that two additional computational models have been analyzed with "moderate" and "strong" vortices, where the moderate vortices generated long neck distortions of the flame sheet and strong vortices produce pinching of necks into pockets that continue to burn within the burnt products. As discussed in Paes,[13] there were few findings that add significantly to what has been discussed here. Primarily, it was found that the stronger-vortex cases emphasize the kinematic Fourier–physical space relationships associated with strongly corrugated flame sheets. Specifically, the variance content of flame corrugations (red spectral regions in Fig. 19) increases relative to the vortices. In addition, the star-like pattern becomes buried within frontal contributions induced by discontinuities at the surfaces of the pockets, which radiate in all directions and obscure the directions of larger-area flat portions of the primary flame sheet. Extrapolating to fully developed turbulence, one anticipates that the star-like pattern observed distinctly (Figs. 11 and 12) becomes a roughly isotropic distribution of star-like patterns. In the current study, we learn that individual kinematic contributions to the Fourier space structure from the frontal content in the presence of the full range of turbulence scales can be extracted with the application of elliptical filters extended to 3D Fourier space similar to the application of three-dimensional wavelet filtering with physically modeled wavelet scales (see the work of Brasseur and Wang,[5] for example).

The current analysis provides a deeper understanding of key SFS modeling dynamics in LES of turbulent reacting flows, where the RS response to the injection of thermal energy well below grid scale cannot be directly predicted and cannot be modeled assuming classical forward-cascade-dominant dynamics where SFS impacts on RS evolution are largely diffusive. Section IV in the current study provides a deeper understanding of the interscale coupling issues that must be considered in advanced closure strategies. We show, for example, that the SFS variance of all variables analyzed is associated with the SFS content of the corrugated flame front. In 2D Fourier space, the flame front lies within the spectral star-like coherent structure, a structure that resides partially in the resolved scales and partially in the subfilter scales. One might therefore anticipate potentially important RS–SFS couplings among the Fourier modes associated with this multiscale coherent structure. We aim to follow the current report with an equally extensive report of the nonlinear couplings associated with the physical–Fourier space coherent structures described in the current study.

## ACKNOWLEDGMENTS

This investigation was funded by the US AFOSR Grant No. FA9550-16-1-0388 under the Basic Combustion Research Program monitored by Dr. Chiping Li and the Computational Mathematics Program monitored initially by Dr. Jean-Luc Cambier and later by Dr. Fariba Fahroo. This work used the Extreme Science and Engineering Discovery Environment (XSEDE), which is supported by the National Science Foundation (Grant No. TG-CTS150017), and the Advanced Cyber Infrastructure computational resources provided by the Institute for CyberScience at the Pennsylvania State University.

## APPENDIX A: REPRESENTATION IN PHYSICAL AND FOURIER SPACE OF HIGHER-ORDER BOUNDARY DISCONTINUITIES OF NONPERIODIC SIGNALS IN FINITE DOMAINS

Consider an arbitrary smooth and continuous 1D signal $f(x)$ over a finite domain $0 \le x \le L$ with boundary values $f(0)$ and $f(L)$. As discussed in Sec. II, if $f(L) \neq f(0)$, the periodic extension of $f(x)$ has a $C^0$ discontinuity at its boundaries with a finite jump $\Delta f = f(L) - f(0)$. As shown in Eq. (3), the $C^0$ discontinuity is


© Author(s) 2021

characterized by a linear "discontinuity function" $d(x)$ with Fourier coefficients $\widehat{d}(k_x)$ that have power-law dependence as $k_x$ [Eq. (2)]. This description may be generalized to higher order boundary discontinuities $C^N$ with jumps in the $n$th derivative $f^{(n)}(x) \equiv d^n f/dx^n$ at the boundary given by $\Delta f^{(n)} = f^{(n)}(L) - f^{(n)}(0)$. These higher order discontinuities are represented in physical space by linear discontinuity functions at the $^{(n)}$ derivative level of $f(x)$, which, when integrated back to the $^{(0)}$ derivative level of $f(x)$, result in $n$th order polynomials.

Similarly to the $C^0$ discontinuity function given by Eqs. (3) and (2), we define the $C^N$ discontinuity function at the derivative level $^{(n)}$ as $d_N^{(n)}(x)$. By construction, the $C^N$ discontinuity function at its highest derivative level ($n = N$) contains the same discontinuity as $f^{(N)}(x)$ separated by a linear function as per Eq. (3) at the functional level,

$$d_N^{(N)}(x) = \frac{\Delta f^{(N)}}{L} x + \mathbb{C}_N^{(N)}. \tag{A1}$$

To construct the $C^N$ discontinuity function at the function level $d_N^{(0)}(x)$ ($n = 0$), $d_N^{(N)}(x)$ is integrated sequentially from $d_N^{(N)}(x)$ to $d_N^{(N-1)}(x)$ and then to $d_N^{(N-2)}(x)$, $d_N^{(N-3)}(x)$, $\ldots d_N^{(n)}(x)$, $\ldots$, ending at the function level $d_N^{(0)}(x)$. At each integration level, a new constant of integration is introduced. These are found with three requirements. First, the discontinuity in the integrated discontinuity function at level $d_N^{(n)}(x)$ must equal the discontinuity in the $n$th derivative in the function $f(x)$ at the $n$th level,

$$\Delta d_N^{(n)} \equiv d_N^{(n)}(L) - d_N^{(n)}(0) = \Delta f^{(n)}. \tag{A2}$$

Second, at the functional ($n = 0$) level, all discontinuity functions must have the same boundary values so that at $x = 0$, $d_N^{(0)}(0) = d_{N-1}^{(0)}(0) = d_{N-2}^{(0)}(0) = d_0^{(0)}(0)$. Finally, as discussed in context with Eq. (2), the discontinuity function at the functional level has zero mean so that $\widehat{d_N^{(0)}}(k_x = 0) = 0$. The result is a collection of polynomial functions $d_N^{(0)}(x)$ that contain $C^{M \le N}$ discontinuities at the boundaries, $M = 0, \ldots, N$.

Using the approach just described, the $C^0$ discontinuity is represented by a linear function at its $n = N = 0$ derivative level,

$$d_0^{(0)}(x) = \frac{\Delta f^{(0)}}{L} x + \mathbb{C}_0^{(0)} = \frac{\Delta f^{(0)}}{L}\left(x - \frac{L}{2}\right), \tag{A3}$$

where the constant is $\mathbb{C}_0^{(0)} = -\frac{\Delta f^{(0)}}{2}$ so that $d_0^{(0)}(x)$ has zero mean (Sec. II A).

Similarly, the $C^1$ discontinuity is represented by a linear function at the $n = N = 1$ derivative level,

$$d_1^{(1)}(x) = \frac{\Delta f^{(1)}}{L} x + \mathbb{C}_1^{(1)}, \tag{A4}$$

which when integrated results in

$$d_1^{(0)}(x) = \int d_1^{(1)} dx + \mathbb{C}_1^{(0)} = \frac{\Delta f^{(1)}}{L} \frac{x^2}{2} + \mathbb{C}_1^{(1)} x + \mathbb{C}_1^{(0)}, \tag{A5}$$

where $\mathbb{C}_1^{(0)} = \mathbb{C}_0^{(0)} = -\frac{\Delta f^{(0)}}{2}$ is obtained by requiring that $d_1^{(0)}(0) = d_0^{(0)}(0)$. The constant $\mathbb{C}_1^{(1)}$ is found by requiring that $\Delta d_1^{(0)} = \Delta f^{(1)}$ in Eq. (A5) so that $\mathbb{C}_1^{(1)} = \frac{\Delta f^{(0)}}{L} - \frac{\Delta f^{(1)}}{2}$. Thus, the $C^0$ and $C^1$ boundary discontinuities in $f(x)$ are represented by a combination of parabolic and linear functions,

$$d_1^{(0)}(x) = \frac{\Delta f^{(1)}}{L} x\left(\frac{x - L}{2}\right) + d_0^{(0)}(x). \tag{A6}$$

We now represent the $C^2$ discontinuity by a linear function at the $n = N = 2$ derivative level,

$$d_2^{(2)}(x) = \frac{\Delta f^{(2)}}{L} x + \mathbb{C}_2^{(2)}. \tag{A7}$$

When integrated twice, this produces

$$d_2^{(1)}(x) = \int d_2^{(2)} dx + \mathbb{C}_2^{(1)} = \frac{\Delta f^{(2)}}{L} \frac{x^2}{2} + \mathbb{C}_2^{(2)} x + \mathbb{C}_2^{(1)} \tag{A8}$$

and

$$d_2^{(0)}(x) = \int d_2^{(1)} dx + \mathbb{C}_2^{(0)} = \frac{\Delta f^{(2)}}{L} \frac{x^3}{6} + \mathbb{C}_2^{(2)} \frac{x^2}{2} + \mathbb{C}_2^{(1)} x + \mathbb{C}_2^{(0)}, \tag{A9}$$

where $\mathbb{C}_2^{(0)} = \mathbb{C}_1^{(0)} = \mathbb{C}_0^{(0)} = -\frac{\Delta f^{(0)}}{2}$ by setting $d_2^{(0)}(0) = d_1^{(0)}(0) = d_0^{(0)}(0)$.

The constant $\mathbb{C}_2^{(2)}$ is found by requiring that $\Delta d_2^{(1)} = \Delta f^{(1)}$ in Eq. (A8) so that $\mathbb{C}_2^{(2)} = \frac{\Delta f^{(1)}}{L} - \frac{\Delta f^{(2)}}{2}$. Similarly, $\mathbb{C}_2^{(1)}$ is found by requiring that $\Delta d_2^{(0)} = \Delta f^{(0)}$ in Eq. (A9) so that $\mathbb{C}_2^{(1)} = \frac{\Delta f^{(0)}}{L} - \frac{\Delta f^{(1)}}{2} + \Delta f^{(2)} \frac{L}{12}$. Thus, the $C^0$, $C^1$, and $C^2$ boundary discontinuities in $f(x)$ are represented by a combination of polynomial discontinuity functions,

$$d_2^{(0)}(x) = \frac{\Delta f^{(2)}}{L} x\left(\frac{x^2}{6} - \frac{xL}{4} + \frac{L^2}{12}\right) + d_1^{(0)}(x). \tag{A10}$$

The procedure to represent the fundamental discontinuities at the boundaries in physical space may be extended to arbitrary order discontinuities $C^{1 \le M \le N}$ as previously discussed. First, the $C^N$ discontinuity is represented by a linear function $d_N^{(N)}(x)$ at the $n = N$ derivative level as per Eq. (A1), which introduces an arbitrary constant $\mathbb{C}_N^{(N)}$. This linear function is incrementally integrated $N$ times to recover the polynomial $d_N^{(0)}(x)$ at the $^{(0)}$ derivative level, which introduces $N$ arbitrary constants $\mathbb{C}_N^{(M)}$ associated with the integrated functions $d_N^{(M)}$ for $M = N - 1, \ldots, 0$, respectively. The constant $\mathbb{C}_N^{(0)} = \mathbb{C}_0^{(0)} = -\frac{\Delta f^{(0)}}{2}$ is obtained by requiring that $d_N^{(0)}(0) = d_0^{(0)}(0)$. Starting at the highest $M$ level of $\Delta d_N^{(M)}$, each unknown constant $\mathbb{C}_N^{(M)}$ is found by requiring that $\Delta d_N^{(M)} = \Delta f^{(M)}$ in the respective integrated level of $d_N^{(N)}(x)$ as per Eq. (A2).

In Fourier space, Eq. (1) may be generalized to $f^{(n)}(x)$,

$$\begin{aligned}\widehat{f^{(n)}}(k_x \neq 0) &= \frac{1}{L}\int_0^L f^{(n)}(x) e^{-ik_x x} dx \\ &= -\frac{i}{k_x}\widehat{f^{(n+1)}}(k_x) + \frac{i}{k_x}\frac{\Delta f^{(n)}}{L}.\end{aligned} \tag{A11}$$


© Author(s) 2021

The fundamental $C^{M\le N}$ discontinuities at the boundaries are therefore represented in Fourier space as

$$\widehat{d_N^{(0)}}(k_x \neq 0) = \sum_{n=0}^{N} \frac{\Delta f^{(n)}}{L}\left(\frac{i}{k_x}\right)^{n+1}, \quad N \geq 0, \tag{A12}$$

where $\widehat{d_N^{(0)}}(0) = 0$.

## APPENDIX B: EXTENSION OF "DISCONTINUITY POLLUTION REMOVAL" PROCEDURE TO MULTIDIMENSIONAL SIGNAL

### 1. Basic strategy

To apply the multidimensional Fourier description to the nonperiodic signals described in Sec. III C, the nonphysical spectral content that arises from discontinuities at the boundaries in $x$ must be removed using the "discontinuity pollution removal" procedure described in Sec. II C. Here, we extend the procedure to multidimensional signals with only one nonperiodic direction. Whereas we develop the generalization to 3D signals, the application to 2D is straightforward.

Consider an analytic 3D signal $f(x,y,z)$ bounded between $(0,0,0)$ and $(L_x,L_y,L_z)$. The signal is periodic in $y$ and $z$ and nonperiodic in $x$ so that the boundary discontinuity $\Delta f(y,z) = f(L_x,y,z) - f(0,y,z)$ can vary with $(y,z)$. There are two ways that the discontinuity removal process in $x$ described in Sec. II C might be applied. In the first, the 1D procedure developed there is applied independently along $x$ pencils at discretized $(y,z)$ locations on the transverse plane. This, however, leads to discontinuities in the modified signal over the $(y,z)$ plane that we would like to avoid. We therefore apply the second method, whereby the 1D procedure described in Sec. II C is developed for the two-dimensional bounded FTF of $f(x,y,z)$ in $y$ and $z$,

$$\widehat{f}^{y,z}(x;k_y,k_z) \equiv FTF_{y,z}\{f(x,y,z)\}, \tag{B1}$$

where we use the hat with adjacent coordinates to indicate the taking of a Fourier transform in the $(y,z)$ coordinate directions. The Fourier coefficients are complex functions defined at discrete transverse wavevectors with discrete components $(k_y,k_z)$ that contain the boundary jumps in x reflecting nonperiodicity as a function of $(k_y,k_z)$. In this way, the discontinuity removal process is decomposed in terms of spatial scale globally over the transverse plane.

Following the procedure in Sec. II A, integration by parts of the Fourier transform of Eq. (B1) in the nonperiodic direction $x$ is

$$\begin{aligned}\widehat{\widehat{f}^{y,z}}^{x}(k_x;k_y,k_z) &= \frac{1}{L_x}\int_0^{L_x}\widehat{f}^{y,z}(x;k_y,k_z)e^{-ik_x x}dx \\ &= -\frac{i}{k_x}\widehat{\frac{\partial \widehat{f}^{y,z}}{\partial x}}^{x}(k_x;k_y,k_z) + \frac{i}{k_x}\frac{\Delta\widehat{f}^{y,z}(k_y,k_z)}{L_x}\end{aligned} \tag{B2}$$

for $k_x \neq 0$, where we use the second hat with adjacent coordinate $x$ to indicate the Fourier transform is in $x$. The "discontinuity function" is therefore

$$\widehat{\widehat{d}^{y,z}}^{x}(k_x;k_y,k_z) = \frac{i}{k_x}\frac{\Delta\widehat{f}^{y,z}(k_y,k_z)}{L_x} \text{ for } k_x \neq 0, \tag{B3}$$

with $\widehat{\widehat{d}^{y,z}}^{x}(0;k_y,k_z) = 0$ (zero mean in $x$). This has the following inverse transform in $x$:

$$\widehat{d}^{y,z}(x;k_y,k_z) = \frac{\Delta\widehat{f}^{y,z}(k_y,k_z)}{L_x}\left(x - \frac{L}{2}\right). \tag{B4}$$

Thus, the discontinuity function in Fourier space, $\widehat{\widehat{d}^{y,z}}^{x}(k_x;k_y,k_z)$, is represented in physical space by a sawtooth function with zero mean. However, unlike the treatment for real 1D functions in Sec. II, here the discontinuity function is complex similar to the 2D Fourier transform of $f(x,y,z)$.

Following the developments in Sec. II C, to localize near the discontinuities at the boundaries, $\widehat{d}^{y,z}(x;k_y,k_z)$ is high-pass filtered to produce a modified discontinuity function with suppressed low-wavenumber contributions from the linear ramp in the discontinuity function between the two boundaries,

$$\widehat{\widehat{d_m}^{y,z}}^{x}(k_x;k_y,k_z,k_{cut}) = m(k_x;k_{cut})\widehat{\widehat{d}^{y,z}}^{x}(k_x;k_y,k_z), \tag{B5}$$

where $m(k_x;k_{cut})$ is the high-pass filter, equal to one when $k_x \geq k_{cut}$ and zero when $k_x < k_{cut}$. Note that $k_{cut} = k_{cut}(k_y,k_z)$, so $k_{cut}$ is determined for each discrete wavevector $(k_y,k_z)$ on the plane perpendicular to the nonperiodic direction. The inverse transform in $x$ of Eq. (B5) returns the function to physical space variations in $x$,

$$\widehat{d_m}^{y,z}(x;k_y,k_z,k_{cut}) = FTF_x^{-1}\left\{\widehat{\widehat{d_m}^{y,z}}^{x}(k_x;k_y,k_z,k_{cut})\right\}. \tag{B6}$$

$\widehat{d_m}^{y,z}(x;k_y,k_z,k_{cut})$ is a modified version of the discontinuity function that localizes to the discontinuities and suppresses the linear ramp of the sawtooth.

Once a useful optimization algorithm is developed to determine $k_{cut}(k_y,k_z)$ (below), the FTF of the original signal $f(x,y,z)$ is modified to remove the spectral content arising from the $x$ boundary discontinuities within $f$,

$$\begin{aligned}\widehat{\widehat{f_m}^{y,z}}^{x}(k_x;k_y,k_z,k_{cut}) = &\widehat{\widehat{f}^{y,z}}^{x}(k_x;k_y,k_z) \\ &- \widehat{\widehat{d_m}^{y,z}}^{x}(k_x;k_y,k_z,k_{cut}).\end{aligned} \tag{B7}$$

In physical space, the modified signal has the form

$$f_m(x,y,z,k_{cut}) = f(x,y,z) - d_m(x,y,z,k_{cut}), \tag{B8}$$

where each term in Eq. (B8) is the 3D inverse Fourier transform of the corresponding Fourier coefficients in Eq. (B7). The residual boundary jump in $x$ in the modified signal is therefore given by

$$\begin{aligned}\Delta f_m(y,z,k_{cut}) &= f_m(L_x,y,z,k_{cut}) - f_m(0,y,z,k_{cut}) \\ &= \Delta f(y,z) - \Delta d_m(y,z,k_{cut}),\end{aligned} \tag{B9}$$

where $\Delta f(y,z)$ and $\Delta d_m(y,z,k_{cut})$ are the boundary jumps in the original signal and modified discontinuity function, respectively. Ultimately, we analyze $\widehat{\widehat{f_m}^{y,z}}^{x}(k_x;k_y,k_z,k_{cut})$ in Fourier space and $f_m(x,y,z,k_{cut})$ in physical space.


© Author(s) 2021

### 2. Algorithm to determine the filter cutoffs

To complete the discontinuity removal process, it is necessary to develop an algorithm to determine the filter cutoff $k_{cut}(k_y,k_z)$ for each discrete wavevector $(k_y,k_z)$. In doing so, one recognizes that because all functions are real in physical space, the reality condition, $\widehat{h}(-k_y^+,-k_z^+)=\widehat{h}^*(k_y^+,k_z^+)$, must be maintained for all functions $h(y,z)$. Thus, for every "positive" wavevector $(k_y^+,k_z^+)$, there exists a "negative" wavevector $(-k_y^+,-k_z^+)$ with a Fourier coefficient determined by the Fourier coefficient of the "positive" wavevector $(k_y^+,k_z^+)$ and $k_{cut}(-k_y^+,-k_z^+)=k_{cut}(k_y^+,k_z^+)$. How one separates the set of wavevectors $(k_y,k_z)$ into the sets $(k_y^+,k_z^+)$ and $(-k_y^+,-k_z^+)$ is, in principle, arbitrary. The algorithm to determine $k_{cut}(k_y,k_z)$ for each $(k_y^+,k_z^+)$ pencil is developed in physical space by extracting the Fourier coefficients in $k_x$ of $\widehat{\widetilde{d}_m}^{y,z^x}(k_x;k_y,k_z,k_{cut})$ and $\widehat{\widetilde{f}_m}^{y,z^x}(k_x;k_y,k_z,k_{cut})$ for each pair of pencils emanating in $x$ from the positive and negative wavevectors, $(k_y^+,k_z^+)$ and $(-k_y^+,-k_z^+)$,

$$\widetilde{h}(x;y,z)=FTF^{-1}_{x,y,z}\left\{\delta(|k_y|-k_y^+,|k_z|-k_z^+)\widehat{\widetilde{h}}^{y,z^x}(k_x;k_y,k_z)\right\}. \quad \text{(B10)}$$

The tilde (˜) implies that the dependence of $\widetilde{h}(x;y,z)$ on $y$ and $z$ comes from a single harmonic Fourier mode selected by the Dirac delta function that defines a sine wave on the $y$–$z$ plane with the wavelength and direction determined by the magnitude and direction of positive/negative wavevector pair associated with the Fourier mode. The $x$-dependence, on the other hand, comes from the $x$-dependence in the nonperiodic direction of the original signal and in $\widehat{\widetilde{h}}^{y,z^x}(k_x;k_y,k_z)\sim\widehat{\widetilde{f}}^{y,z^x}$, $\widehat{\widetilde{d}_m}^{y,z^x}$, and $\widehat{\widetilde{f}_m}^{y,z^x}$ in Eq. (B10), including the residual boundary jump in $\widehat{\widetilde{f}_m}^{y,z^x}$ along scale-based pencils in $x$ at $(k_y^+,k_z^+)$ and $(-k_y^+,-k_z^+)$.

The aim is to minimize the residual boundary jump in $f_m$ [Eq. (B9)] without significantly altering the signal away from the $x$ boundaries. To this end, we follow the approach described in Sec. II C, whereby a weighting parameter $\alpha$ [Eq. (10)] is used to balance two parameters: one designed to quantify the relative change made in the signal away from the boundary [$\varepsilon$, Eq. (7)] and the other designed to quantify the level of residual boundary discontinuity and non-periodicity in $x$ [$\Delta_r$, Eq. (8)] retained in the modified signal, $f_m$. In the multidimensional application, however, these parameters are formed using the form of the function $\widetilde{h}$ in Eq. (B10) that select a single pair of Fourier modes on the $y$–$z$ plane defined by the "positive" mode, $(k_y^+,k_z^+)$,

$$\varepsilon(k_y^+,k_z^+;k_{cut})=\frac{\|\widetilde{d_m}(x,y,z;k_{cut})\|_V}{\|\widetilde{f}(x,y,z)\|_V}, \quad \text{(B11)}$$

$$\Delta_r(k_y^+,k_z^+;k_{cut})=max_{y,z}\left\{\frac{|\Delta\widetilde{f_m}(y,z;k_{cut})|}{|max_x\left(\partial\widetilde{f}(x,y,z)/\partial x\right)|\Delta x}\right\}, \quad \text{(B12)}$$

where $k_{cut}=k_{cut}(k_y^+,k_z^+)$. Both parameters are defined for pencils at $(k_y^+,k_z^+)$ with their conjugate locations $(-k_y^+,-k_z^+)$. In Eq. (B11), $\|\cdots\|_V$ is the $L_2$ norm over volume $V$ within the computational domain, allowing the user to select, if desired, the region that is most critical to minimize deviation in the original signal. In Eq. (B12), $\Delta\widetilde{f_m}(y,z,k_{cut})=\widetilde{f_m}(L_x,y,z,k_{cut})-\widetilde{f_m}(0,y,z,k_{cut})$, defined by inserting $\widehat{\widetilde{f}}^{y,z^x}$ into Eq. (B9) for $\widehat{\widetilde{h}}^{y,z^x}(k_x;k_y,k_z)$, is a function of $(y,z)$. The denominator selects the largest physical $x$ gradient in $\widetilde{f}$ in $x$ away from the boundaries, where $\widetilde{f}$ is defined along $(k_y,k_z)$ pencils. Both the numerator and denominator of the ratio in Eq. (B12) depend on $(y,z)$, and $\Delta_r$ is defined as the maximum value of the ratio in Eq. (B12) over the $y$–$z$ plane.

$\varepsilon(k_y^+,k_z^+;k_{cut})$ and $\Delta_r(k_y^+,k_z^+;k_{cut})$ are both functions of $k_{cut}$, which is itself a function of $(k_y^+,k_z^+)$. As per Sec. II C, we select the optimal value for $k_{cut}$ at each $(k_y^+,k_z^+)$ by identifying the minimum in the following function with a specified weighting parameter, $\alpha$:

$$\phi(k_{cut};\alpha)=\alpha\varepsilon(k_y^+,k_z^+;k_{cut})+(1-\alpha)\Delta_r(k_y^+,k_z^+;k_{cut}). \quad \text{(B13)}$$

The optimal choice for $k_{cut}$ is found at the minimum in $\phi$ as a function of $k_{cut}$ for specified fixed $\alpha$,

$$\phi(k_{cut}^{opt};\alpha)=min_{k_{cut}}[\phi(k_{cut};\alpha)]. \quad \text{(B14)}$$

As described in Sec. II C, $\alpha$ is chosen by the user to balance the degree of reduction of the polluting consequences of the unphysical boundary discontinuity induced by the Fourier transform in the nonperiodic direction with the level of modification to the signal away from the boundary.

The result of applying Eq. (B14) with user-defined $\alpha$ is an optimal value of $k_{cut}$ for each value of $(k_y,k_z)$ as needed to complete the discontinuity removal process extended to multidimensional signals, as described above in Appendix B 1.

## APPENDIX C: VALIDATION AND PARAMETERIZATION OF THE DISCONTINUITY POLLUTION REMOVAL PROCEDURE

The discontinuity removal procedure introduced in Sec. II and formalized for multidimensional signals in Appendix B is validated using the 2D flame–vortex interaction simulation described in Sec. III C. To illustrate the outcome of the procedure, Fig. 25 presents the original ($f$) and modified ($f_m=f-d_m$) signals of $\rho u$ along with its associated modulated discontinuity function, $d_m$, in physical space. The signals are shown over the computational domain ($0\le x/D\le 16$) at the time instant of largest boundary discontinuity in $x$ ($\Delta f$) in $\rho u$, which occurs with the vortices at the inflow and elongated streaks in the products (Sec. III C). Note that in Secs. III C and IV, the signals are analyzed at the time instant when the flame is most "corrugated."

The Fourier space counterparts of the original, post-processed, and modulated discontinuity signals associated with $\rho u$ are presented in Fig. 26. We plot isocontours of the logarithms of squared Fourier coefficients of $\rho u$ with the color bars spanning five orders of magnitude of $\log(\rho u)^2$. The wavenumber axes are normalized using the planar laminar flame thickness. Figure 26 shows 2D Fourier space down to the flame scale, which are the values $k_{x,y}\delta_f/\pi=\pm1$. The pink box identifies the vortex scale defined by $k_{x,y}\delta_f/\pi=\pm\delta_f/D=0.06$, where $k_v\equiv\pi/D$ is the vortex-scale wavenumber [see Fig. 9(b)], the four Fourier modes used to construct the train of vortices at inflow. As explained in Sec. IV, the spanwise symmetry of the inflow vortices leads to negligible Fourier content in Fourier modes odd in $k_y$ (i.e., at $k_y/\Delta k_y=\pm1,\pm3,\ldots$). These odd $k_y$ modes


© Author(s) 2021

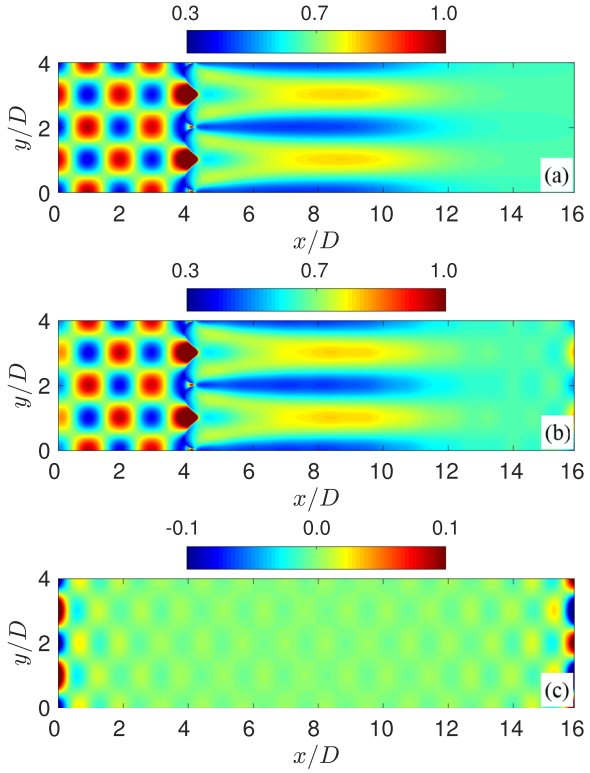


**FIG. 25.** Isocontours of (a) the original signal $f(x, y)$ and (b) the modified signal $f_m(x, y)$ in physical space of $\rho u$ for the 2D flame–vortex interaction simulation. The associated modulated discontinuity function $d_m$ is shown in (c).

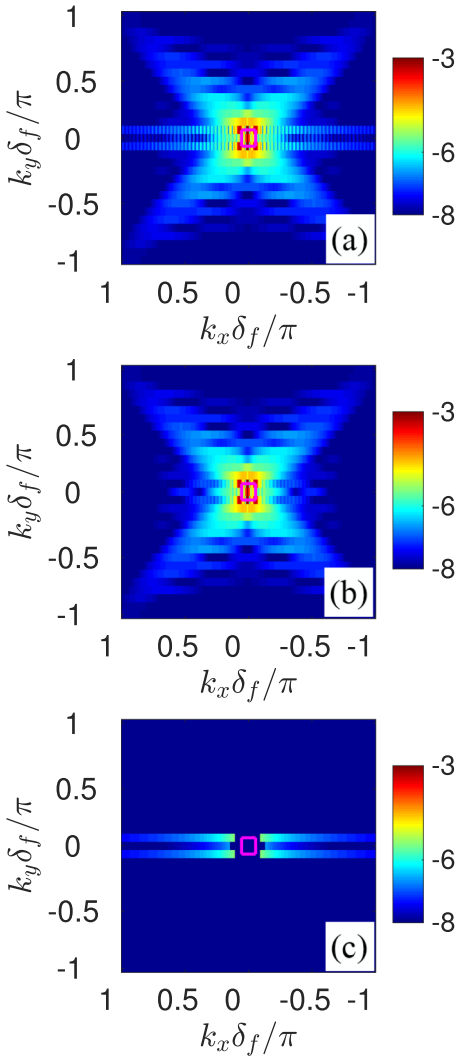


**FIG. 26.** Isocontours of the (a) original $\widehat{f}(k_x; k_y, k_z)$ signal and (b) modified $\widehat{f_m}(k_x; k_y, k_z, k_{cut})$ signal in Fourier space of $\log(\widehat{\rho u^2})$ for the 2D flame–vortex interaction simulation. The associated modulated discontinuity is shown in (c).

have been removed from all spectral isocontour plots to improve the visualization.

The highest magnitude Fourier energy content in Fig. 26(a) includes a "star-like" pattern that extends to the highest wavenumbers, extending from the vortex scale box to the flame scale box aligned at $\pm 42^\circ$ from the $k_x$-axis. In Sec. II A, we showed that discontinuities create power-laws in Fourier space that extend from the lowest wavenumbers to the grid scale, where a discretized discontinuity becomes a large gradient. The star-like pattern in Fig. 26 arises from power-law drops in variance arising from the large physical gradients at the flame front, as described in Sec. IV. While the star-like pattern is associated with physically relevant frontal structures of the signals [i.e., the corrugated flame fronts in Fig. 10(a)], unphysical power-law variations associated with boundary discontinuities are observed in Fig. 26(b) as bands over $k_x$ with large Fourier content at $|k_y|\delta_f/\pi \leq 0.06$ (i.e., at wavenumbers $k_y/\Delta k_y = 0, \pm 2$). These scales are associated with the cross-stream averaged mean ($k_y\delta_f/\pi = 0$) and the transverse scale of the vortices ($k_y\delta_f/\pi = \pm\delta_f/D$), which introduce boundary discontinuities between the inflow and outflow [Fig. 25(a)].

To effectively remove this pollution, the discontinuity removal procedure described in Appendix B was applied with $\alpha = 0.85$, which ensures that the maximum signal modification at the polluted wavenumbers [Eq. (B11)] remains smaller than 5%. The fundamental discontinuity function $d(x, y)$ is constructed considering only the $C^0$ discontinuity [Eq. (B3)], and the volume of interest in Eqs. (B11) and (B12) is the region $2 \leq x/D \leq 8$.

Figures 25(b), 25(c), 26(b), and 26(c) show in physical and Fourier space, respectively, the 2D instantaneous isocontours of the modulated discontinuity function ($d_m$) and the post-processed signal ($f_m = f - d_m$). The modulated discontinuity function in physical space [Fig. 25(c)] minimizes the modification in the signal within the domain and localizes the harmonic functions toward the discontinuities at the boundaries in $x$ with variations at the vortex scale in $y$. Thus, the final signal in physical space [Fig. 25(b)] preserves the original signal [Fig. 25(a)] away from the boundaries. In Fourier space, the modulated discontinuity function [Fig. 26(c)] captures the power-law pollution in $k_x$ at $k_y\delta_f/\pi = 0$ and $\pm 0.06$ with negligible contribution at unpolluted wavenumbers. The optimal cutoff wavenumbers $k_{cut}^{opt}(k_y)$ that modulate the power-laws in


© Author(s) 2021

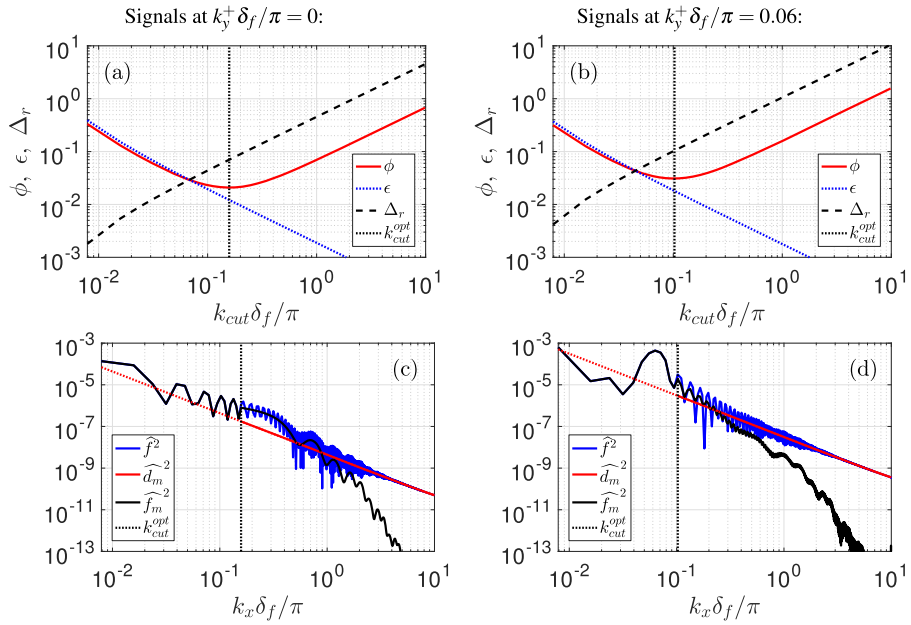


**FIG. 27.** [(a) and (b)] Computed $\phi$, $\varepsilon$, and $\Delta_r$ as functions of $k_{cut}$ for $\alpha = 0.85$ and $V$ in the range $2 \le x/D \le 8$ and [(c) and (d)] squared Fourier coefficients $\widehat{f}^2$, $\widehat{d_m}^2$, and $\widehat{f_m}^2$ as functions of $k_x$, where the dashed red line indicates unmodulated $\widehat{d}^2$. Signals at $k_y^+\delta_f/\pi = 0$ [left: (a) and (c)] and 0.06 [right: (b) and (d)]. The vertical dotted line indicates optimal $k_{cut}$.

Fig. 26(c) are higher than the $k_x$ vortex-scale wavenumbers so that the power-law pollution is removed at scales smaller than the vortex scales ($|k_x|\delta_f/\pi > 0.06$). Consequently, while power-law pollution from the boundary discontinuity is removed in the modulated signal in Figs. 26(b) and 25(b), the large-scale vortex structures and the star-like pattern associated with the corrugated flame front are unaffected.

To access the tradeoff between the signal modification and the residual boundary discontinuity in the selection of the optimal wavenumber cutoffs $k_{cut}^{opt}(k_y^+)$, we analyze the filtered signals at each $k_y^+$ separately [Eq. (B10)]. Figures 27(a) and 27(b) show at fixed $k_y^+\delta_f/\pi = 0$ and 0.06, respectively, the computed $\phi$, $\varepsilon$, and $\Delta_r$ as functions of $k_{cut}$, where the optimal wavenumber cutoff $k_{cut}^{opt}(k_y^+)$ is indicated by the vertical dotted black lines. Figures 27(c), 27(d), 28(a), and b28(b) show, in Fourier and physical space ($y/D = 1$), respectively, the filtered signals associated with $f$, $d_m$, and $f_m$ for $k_y^+\delta_f/\pi = 0$ and 0.06.

In Fourier space, the original signal shows a clear power-law pollution at the highest wavenumbers starting at $k_x\delta_f/\pi \approx 1$ for $k_y^+\delta_f/\pi = 0$ [Fig. 27(c)] and at $k_x\delta_f/\pi \approx 0.2$ for $k_y^+\delta_f/\pi = 0.06$ [Fig. 27(d)]. Above these polluted wavenumbers, $\Delta_r$ crosses 1 in Figs. 27(a) and 27(b) and the Fourier coefficients are modified by the procedure without significant modification of the original signal, as indicated by the values of $\varepsilon < 2\%$. (Note that $\varepsilon$ is as high as 40% at the smallest $k_{cut}$.) The optimal wavenumber cutoffs $k_{cut}^{opt}$ with $\alpha = 0.85$ (vertical black dotted lines in Fig. 27) favor the minimization of signal modification so that $\varepsilon(k_{cut}^{opt}) \sim 1 - 2\%$ and $\Delta_r(k_{cut}^{opt}) \sim 9 - 15\%$ for $k_y^+\delta_f/\pi = 0$ and 0.06. As a result, the Fourier energy of the modified signal in Figs. 27(c) and 27(d) transitions to exponential decay around the flame front thickness ($k_x\delta_f/\pi \approx 1$) with approximate power decay exponents of −8.60 and −7.52, respectively. Thus, the discontinuity removal process has recovered the signal associated with the flame front. As importantly, the Fourier content associated with the vortex scales [the peak in the spectrum of $f$ in Fig. 27(d) at $k_y^+\delta_f/\pi = 0.06$] is preserved.

In Fig. 28, we plot two examples of physical space functions $\widetilde{f}(x,y)$, $\widetilde{d_m}(x,y)$, and $\widetilde{f_m}(x,y)$, filtered as per Eq. (B10) for pencils in $x$ at $k_y^+\delta_f/\pi = 0$ and 0.06, shown as functions of $x/D$ at $y/D = 1$. Variations in $x/D$ are plotted at $y/D = 1$. The modified signal $f_m$ is

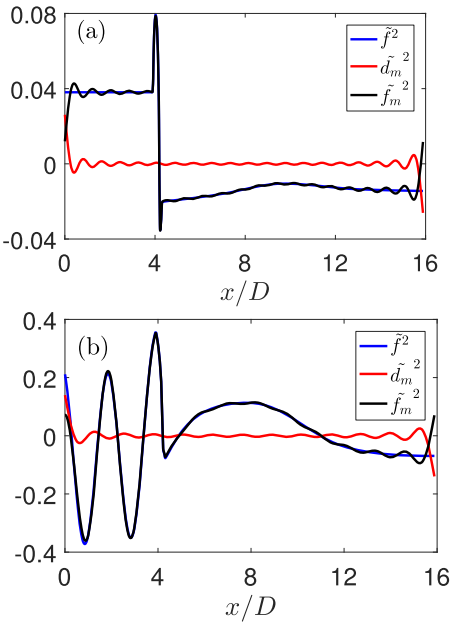


**FIG. 28.** $\widetilde{f}$, $\widetilde{d_m}$, and $\widetilde{f_m}$, filtered as per Eq. (B10) at (a) $k_y^+\delta_f/\pi = 0$ and (b) 0.06, shown as functions of $x/D$ at $y/D = 1$.


© Author(s) 2021

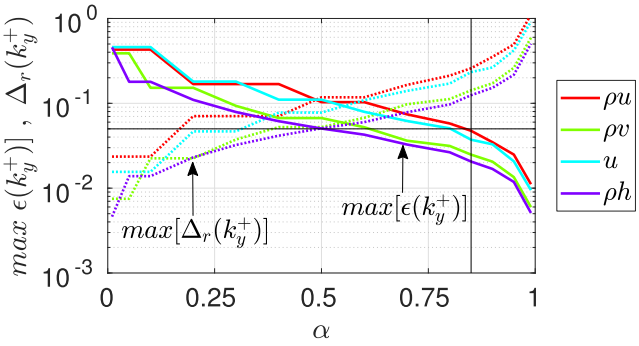


**FIG. 29.** Maximum over $k_y^+$ of $\varepsilon$ (solid curves) and $\Delta_r$ (dashed curves) as a function of $\alpha$ for different variables in the 2D flame–vortex interaction simulation. The vertical lines are at $\alpha = 0.85$.

shown to preserve the original signal away from the boundaries with modification toward the domain boundaries [$\widetilde{d_m}(x;k_y^+)$ in Fig. 28]. The "ripples" result from the sharp filter $m(k_x;k_{cut})$ [Eq. (6)] employed to modulate $\widehat{d}(k_x)$. This kinematic ringing effect can be removed with the use of smooth Fourier space filters (not shown). Note from Fig. 28 that the vortices in the reactants ($x/D < 4$), elongated streaks in the products ($x/D > 4$), and large gradients within the flame front ($x/D \approx 4$) are all preserved in the modified signal.

Figure 29 shows the sensitivity of the maximum $\varepsilon(k_y^+)$ (solid curves) and $\Delta_r(k_y^+)$ (dashed curves) as a function of $\alpha$ for the pollution removal procedure applied to $\rho u$, $\rho v$, $u$, and $\rho h$ from the 2D flame–vortex interaction simulation. Because $\rho Y_{HCO}$ is highly localized within the flame $\Delta f = 0$. Therefore, $d = 0$ zero and the signal is unaffected. The procedure is shown to be robust for distinct variables, and the choice of $\alpha = 0.85$ ensures that the maximum signal modification and residual jump in the post-processed signal for all variables remains smaller than 5% and 30%, respectively, as indicated by the horizontal lines in Fig. 29.

## DATA AVAILABILITY

The data that support the findings of this study are available from the corresponding author upon reasonable request.

## REFERENCES

[1]G. Berkooz, P. Holmes, and J. L. Lumley, "The proper orthogonal decomposition in the analysis of turbulent flows," Annu. Rev. Fluid Mech. **25**, 539–575 (1993).
[2]L. Perret, J. Delville, R. Manceau, and J.-P. Bonnet, "Generation of turbulent inflow conditions for large eddy simulation from stereoscopic PIV measurements," Int. J. Heat Fluid Flow **27**, 576–584 (2006).
[3]C. W. Rowley, I. Mezić, S. Bagheri, P. Schlatter, and D. S. Henningson, "Spectral analysis of nonlinear flows," J. Fluid Mech. **641**, 115–127 (2009).
[4]J. Brasseur, "The wavelet decomposition—Locality in Fourier space, locality in physical space, and the relationship between the two," in *Fluid Dynamics Conference* (AIAA, 1994).
[5]J. G. Brasseur and Q. Wang, "Structural evolution of intermittency and anisotropy at different scales analyzed using three-dimensional wavelet transforms," Phys. Fluids A **4**, 2538–2554 (1992).
[6]M. Farge, "Wavelet transforms and their applications to turbulence," Annu. Rev. Fluid Mech. **24**, 395–458 (1992).
[7]G. K. Batchelor, *The Theory of Homogeneous Turbulence* (Cambridge University Press, 1953).
[8]J. G. Brasseur and W. Lin, "Kinematics and dynamics of small-scale vorticity and strain-rate structures in the transition from isotropic to shear turbulence," Fluid Dyn. Res. **36**, 357 (2005).
[9]J. G. Brasseur and C. H. Wei, "Interscale dynamics and local isotropy in high Reynolds number turbulence within triadic interactions," Phys. Fluids **6**, 842–870 (1994).
[10]P. L. K. Paes, J. Brasseur, and Y. Xuan, "A novel strategy to identify dynamically dominant inter-scale couplings for application to large-eddy simulation of premixed turbulent combustion," in *AIAA Scitech 2019 Forum* (AIAA, 2019).
[11]J. G. Brasseur and S. Corrsin, "Spectral evolution of the Navier-Stokes equations for low order couplings of Fourier modes," in *Advances in Turbulence*, edited by G. Comte-Bellot and J. Mathieu (Springer Berlin Heidelberg, Berlin, Heidelberg, 1987), pp. 152–162.
[12]J. A. Domaradzki and R. S. Rogallo, "Local energy transfer and nonlocal interactions in homogeneous, isotropic turbulence," Phys. Fluids A **2**, 413–426 (1990).
[13]P. L. K. Paes, "Analysis of inter-scale turbulence-chemistry dynamics with reduced physics simulations for application to large-eddy simulation of premixed turbulent combustion," Ph.D. thesis, The Pennsylvania State University, 2018.
[14]P. L. K. Paes, J. Brasseur, and Y. Xuan, "Kinematic relationships between physical and Fourier space in premixed turbulent combustion for application to large-eddy simulation," in *AIAA Scitech 2019 Forum* (AIAA, 2019).
[15]I. Daubechies, *Ten Lectures on Wavelets Regional*, Conference Series in Applied Mathematics (Society for Industrial and Applied Mathematics, 1992).
[16]C. S. Carrano, Jr., "General decompositions and spectral dynamics applied to Burgers' model of turbulence," Ph.D. thesis, The Pennsylvania State University, 1997.
[17]N. E. Huang, Z. Shen, S. R. Long, M. C. Wu, H. H. Shih, Q. Zheng, N.-C. Yen, C. C. Tung, and H. H. Liu, "The empirical mode decomposition and the Hilbert spectrum for nonlinear and non-stationary time series analysis," Proc. R. Soc. London, Ser. A **454**, 903–995 (1998).
[18]J. Kim, M. Bassenne, C. A. Z. Towery, P. E. Hamlington, A. Y. Poludnenko, and J. Urzay, "Spatially localized multi-scale energy transfer in turbulent premixed combustion," J. Fluid Mech. **848**, 78–116 (2018).
[19]P. L. Paes and Y. Xuan, "Numerical investigation of turbulent kinetic energy dynamics in chemically-reacting homogeneous turbulence," Flow, Turbul. Combust. **101**, 775–794 (2018).
[20]L. A. D. Hutchison and W. A. Barrett, "Fourier–Mellin registration of line-delineated tabular document images," Int. J. Doc. Anal. Recognit. **8**, 87 (2006).
[21]F. J. Harris, "On the use of windows for harmonic analysis with the discrete Fourier transform," Proc. IEEE **66**, 51–83 (1978).
[22]J. D. Villasenor, "Alternatives to the discrete cosine transform for irreversible tomographic image compression," IEEE Trans. Med. Imaging **12**, 803–811 (1993).
[23]J. M. Foucaut, J. Carlier, and M. Stanislas, "PIV optimization for the study of turbulent flow using spectral analysis," Meas. Sci. Technol. **15**, 1046 (2004).
[24]O. P. Bruno, Y. Han, and M. M. Pohlman, "Accurate, high-order representation of complex three-dimensional surfaces via Fourier continuation analysis," J. Comput. Phys. **227**, 1094–1125 (2007).
[25]L. Moisan, "Periodic plus smooth image decomposition," J. Math. Imaging Vision **39**, 161–179 (2011).
[26]P. L. K. Paes, Y. G. Shah, J. G. Brasseur, and Y. Xuan, "A scaling analysis for the evolution of small-scale turbulence eddies across premixed flames with implications on distributed combustion," Combust. Theory Modell. **24**, 307–325 (2020).
[27]R. Borghi, "On the structure and morphology of turbulent premixed flames," in *Recent Advances in the Aerospace Sciences, in Honor of Luigi Crocco on his Seventy-fifth Birthday* (Springer US, Boston, MA, 1985), pp. 117–138.
[28]N. Peters, *Turbulent Combustion* (Cambridge University Press, 2000).
[29]F. A. Williams, *Combustion Theory: The Fundamental Theory of Chemical Reacting Flow Systems* (Addison-Wesley, 1965).


© Author(s) 2021

[30]A. W. Skiba, T. M. Wabel, C. D. Carter, S. D. Hammack, J. E. Temme, and J. F. Driscoll, "Premixed flames subjected to extreme levels of turbulence part I: Flame structure and a new measured regime diagram," Combust. Flame **189**, 407–432 (2017).
[31]T. Poinsot, D. Veynante, and S. Candel, "Quenching processes and premixed turbulent combustion diagrams," J. Fluid Mech. **228**, 561–606 (1991).
[32]S. A. Filatyev, J. F. Driscoll, C. D. Carter, and J. M. Donbar, "Measured properties of turbulent premixed flames for model assessment, including burning velocities, stretch rates, and surface densities," Combust. Flame **141**, 1–21 (2005).
[33]O. Desjardins, G. Blanquart, G. Balarac, and H. Pitsch, "High order conservative finite difference scheme for variable density low Mach number turbulent flows," J. Comput. Phys. **227**, 7125–7159 (2008).
[34]S. Verma, Y. Xuan, and G. Blanquart, "An improved bounded semi-Lagrangian scheme for the turbulent transport of passive scalars," J. Comput. Phys. **272**, 1–22 (2014).
[35]B. Savard, Y. Xuan, B. Bobbitt, and G. Blanquart, "A computationally-efficient, semi-implicit, iterative method for the time-integration of reacting flows with stiff chemistry," J. Comput. Phys. **295**, 740–769 (2015).
[36]B. Bobbitt, S. Lapointe, and G. Blanquart, "Vorticity transformation in high Karlovitz number premixed flames," Phys. Fluids **28**, 015101 (2016).
[37]S. Lapointe, B. Savard, and G. Blanquart, "Differential diffusion effects, distributed burning, and local extinctions in high Karlovitz premixed flames," Combust. Flame **162**, 3341–3355 (2015).
[38]G. Blanquart, P. Pepiot-Desjardins, and H. Pitsch, "Chemical mechanism for high temperature combustion of engine relevant fuels with emphasis on soot precursors," Combust. Flame **156**, 588–607 (2009).
[39]F. Bisetti, G. Blanquart, M. E. Mueller, and H. Pitsch, "On the formation and early evolution of soot in turbulent nonpremixed flames," Combust. Flame **159**, 317–335 (2012).
[40]H. N. Najm, P. H. Paul, C. J. Mueller, and P. S. Wyckoff, "On the adequacy of certain experimental observables as measurements of flame burning rate," Combust. Flame **113**, 312–332 (1998).
[41]C. Mueller, J. F. Driscoll, D. L. Reuss, M. C. Drake, and M. E. Rosalik, "Vorticity generation and attenuation as vortices convect through a premixed flame," Combust. Flame **112**, 342–358 (1998).
[42]D. S. Louch and K. N. C. Bray, "Vorticity and scalar transport in premixed turbulent combustion," Symp. (Int.) Combust. **27**, 801–810 (1998).


© Author(s) 2021